Department of Energy
DOE Grant No. DE-FG03-01ER83297

Novel Neutron Detector for High Rate Imaging Applications

Final Report

Proportional Technologies, Inc.

August 27, 2004

List of Tables

List of Figures

1 Phase II Study

The Phase II period performance was May 30, 2002 through May 29, 2004. This development effort was successfully completed within the period and budget allotted. The proposed design was successfully fabricated from B_4C-coated aluminum and copper film, slit and wound to form 4 mm diameter straws, cut to 100 cm in length, and threaded with resistive anode wires (20 μm in diameter). The following paragraphs report testing done with two 50-straw detector modules at the reactor of the Nuclear Science Center at Texas A&M University (TAMU NSC).

Detector description. Two prototype detector modules were fabricated and tested. Each module consists of a close-packed array of 50 straws, that can mate in turn in close-packed fashion with neighboring modules, as shown in the schematic drawing of Fig. 1. Such close packing can be carried to as many modules as desired to produce any desired continuous detection volume within a secondary housing. Each straw is 100 cm long and only 4 mm in diameter, it is made by winding thin strips of either aluminum or copper, and incorporates a micron-thick layer of boron carbide (B_4C) on the inner surface of the inner layer. A picture of the two complete modules forming a closely packed array of 100 straws is shown in Fig. 2. The two detectors are shown inside their aluminum housing in Fig. 3. The sensitive face area of the two modules combined was 800 cm^2, and their depth in the direction of irradiation was 1.73 cm. The following paragraphs give details on their construction.

Straws are manufactured using a high speed winding technique in which narrow ribbons of aluminum or copper film are helically wound around a cylindrical mandrel of precise dimension. Quickset adhesive, applied to the film on the fly, instantly bonds the multiple layers of film together. In this manner, large quantities can be produced at high rate and thus low cost. The technical team identified a company (Lamina Dielectrics, Ltd.) that is the world leader in this winding process for straws used in HEP as well as for other applications, such as wire insulation.

A resistive anode wire 20 μm in diameter is tensioned in the center of each straw. All 50 straws and wires terminate in a dual board assembly that electrically connects all cathodes together, provides electrical insulation between the straw wall and the wires, and allows for gas flow, as shown in the schematic of Fig. 4. This assembly structure includes two fiberglas circuit boards, a cathode board and an anode board, shown in Fig. 5, that mate together to create a gas-tight cavity. The straw end fittings form an open connection to the resulting chamber, which is fed by a single gas input/output port. In this manner, effective gas flow was achieved. Electrical contact between the anode wire and the board was achieved using a low-cost standard diameter copper tube. A copper tube was soldered in each hole of the anode board, thereby establishing electrical connection and fixation. The design was also compatible with efficient threading, tensioning, and attachment of the anode wire.

Assembly of straws into honeycomb-like arrays proved quite feasible by constructing individual rows, which were then stacked vertically. After inserting the end fitting inside the straws, straws were arranged adjacent to each other atop a granite slab to ensure linearity. An alignment device gently held the straws in place while they were bonded together using spot application of fast setting cement applied with a hypodermic syringe. Each layer was then positioned so that straws fit into grooves created by the top of the underlying row. This assembly technique produces very sturdy arrays.

In the first step of module assembly, the straw array was connected to the cathode board. Conductive epoxy was liberally applied to the inside surfaces of the holes in the board, and the straw array was plugged into board. The displacement of excess epoxy produced a conductive layer on the outer surface of the board, thereby providing connection to the cathodes. This process

was performed for both ends of the array. The connection provided a secure seal, preventing gas leakage, and helped to maintain structural integrity. After the detectors were firmly attached to the cathode board, the anode board was mated to the cathode board to create a gas-tight seal.

Another advantage offered by this module design was a simple technique for wire threading and tensioning. This technique allowed these steps to be performed for the entire array in a quick and efficient manner using the apparatus shown in Fig. 6. A module, consisting of a straw array with a dual-board assembly structure mounted on each end, was positioned horizontally and clamped in place. An air blowing system was implemented by connecting compressed helium (15 psi) through a plastic hose to a length of small diameter tube. For each straw in the array, the tube was positioned over a hole in the anode board (with copper tube already in place), through the chamber, and down to the Ultem end fitting, creating a columnar gas flow through the tube and the straw. Stablohm 800 resistance anode wire (California Fine Wire Co.) of diameter 20 μm was threaded through each straw using an air jet technique. Fixation and electrical connection were achieved by soldering the wire at each end inside small diameter copper tubes. After soldering one end of the wire tensioning was achieved using a small weight hanging over a pulley and the second end of the wire was soldered.

To further support the anode wire, a twister was placed in a plastic sleeve and affixed to the center of each straw of the module. This effectively doubled the allowable anode length for a given wire tension while still maintaining electrostatic stability. The maximum operating voltage achieved with this twister was more than four times the operational voltage and thus should not be necessary in production devices since a two-fold safety factor is achieved without the twister. However, in this initial evaluation it was considered prudent to implement this additional margin of safety.

Experimental Setup. The neutron beam port at the NSC was located inside a "cave", consisting of a long shielded corridor with roof access, as shown in Fig. 7. The detector and attached collimator were placed in the cave hanging from the roof, as shown in Fig. 8, a distance of 3.35 m away from the beam port opening. All signal and high voltage cables were run through a conduit to a nearby shielded radiography room. Testing equipment, shown in Fig. 9, was setup in this room, and included high voltage supplies, discriminators, an oscilloscope, the data acquisition system, and computers. Also, from this room the reactor control room could be contacted to set the desired power level of the reactor. The computer and data acquisition system digitized and stored anode signals from both ends of the detector for each event. The cathode signal was used to trigger the acquisition. Various experiments were performed using different collimators and reactor power levels. For all experiments, the detectors were biased to 1150 V, and the gas mixture employed was argon/methane (90/10). Due to the limited size of the neutron beam, only half of the detector length (50 cm) could be irradiated at a time. Thus, most experiments involved moving the detector to one of two positions, then repeating at the other position. One of the more notable deficiencies of the study turned out to be caused by unexpected degradation of neutron beam quality at the edges of the beam. Detector resolution was seen to degrade substantially in these halo regions indicating that resolution results can only be taken as worst case measurements, and that true detector resolution will be significantly better. A summary of the experiments is shown in Table 1.

Readout. The detector readout was divided up into two stages: front-end and digitization electronics. Front-end electronics consisted of pre-amplifiers and filters on each end of the anode wires, as well as a cathode amplifier used for triggering the digitization system. Figure 10 shows a schematic of the setup. Anode signals were terminated into the virtual ground of current-sensitive pre-amps using 330 ohms termination resistors. The terminating value of 330 ohms was found to

be optimal in preventing signal reflection. The anode and cathode pre-amps utilize the National Semiconductor LMH6624 chip, which is an ultra low noise (0.92 nV/$\sqrt{\text{Hz}}$, 2.3 pA/$\sqrt{\text{Hz}}$), wideband (1.5 GHz) operational amplifier. Anode signals were further conditioned by a 3-pole low-pass filter to remove high frequency noise outside the signal bandwidth, before being digitized.

Anode and cathode signals are then sent to a proprietary digitization system, manufactured by A&D Precision Co. The system is highly scalable, allowing it to read out many detectors with very little change in software or hardware. The unit features 12-bit charge-integrating ADCs to digitize anode signals, as well as a discriminator to trigger the unit based on the cathode input. Once data was digitized, it was formed into Ethernet packets and sent to a host computer via a Gigabit switch. Control software written in C++ was used to acquire the data and store it into files for analysis with MATLAB. All readout components were portable and were set up at NSC for the duration of the experimental evaluation.

Longitudinal position was measured using a charge (current) division method. When a signal is produced in a straw, the current splits in inverse proportion to the distance from the end of the straw, producing a signal from each end (A and B). The longitudinal coordinate was obtained by taking the ratio of $A/(A+B)$.

Straw decoding was accomplished by tieing groups of either rows or columns of straws together into delay line taps and timing the delay line outputs to determine into which tap current was injected. On one end of the detector, straws were tied together in rows (row decoding end) and on the other side, they were connected in columns (column decoding end), as shown in Fig. 10. When an event occurs in a straw, its current divides and is injected into a tap of the row delay line and a tap of the column delay line. By timing the outputs of the delay lines, both a row and column number can be obtained, thus identifying the straw in which the event was detected. By combining this information with the longitudinal position measured using charge division, a full 3D position can be obtained for each detected event.

The signals from each end of the delay lines are amplified, filtered, and passed to a custom-made readout system which timed the delay line outputs. Also, the outputs of each delay line were summed together to measure the total charge delivered to each end of the detector that will be used for calculating the longitudinal position. The readout system was equipped with 14-bit ADCs for measuring charge (longitudinal position) and 12-bit TDCs for timing (straw decoding). The system is highly scalable and is currently capable of reading 8 50-straw detectors simultaneously. It can operate at a rate approaching 5 MHz and transfers data to a PC using a Gigabit Ethernet link. The PC used was running RedHat Linux 7.1.

Gas Multiplication & Energy Resolution The prototype detector was operated in a mode of proportional amplification, whereby maximum signal levels were achieved while maintaining adequate energy resolution. The gas mixture used was 90% argon and 10% methane, and the resulting amplification factor is shown in Fig. 11. Measurement of the amplification factor was done by placing a 37 MBq (1 mCi) ^{55}Fe gamma source next to a single straw detector, filled with a gas mixture of 90% argon and 10% methane, and recording the count rate and corresponding average ionization current. The ratio of the two numbers measures the amplified charge generated due to avalanching. The detector showed stable operation up to a bias level of 1200 V, with a corresponding multiplication factor of 50,000, and without significant degradation in energy resolution. The breakdown point was at 1550 V.

Figure 12 shows energy spectra collected with a moderated ^{252}Cf source at different bias voltages. Neutron and gamma events deposit markedly different amounts of energy in the detector, with most neutron events depositing energies significantly higher than those of gamma events, as indicated in

the figure (bottom panel). Gamma discrimination is easily achieved by setting an energy threshold above the gamma tail.

Neutron Detection Efficiency The detection efficiency for thermal neutrons was measured with both the copper and aluminum straw modules positioned in the neutron beam of the TAMU NSC reactor in the orientation shown in Fig. 1. The intensity of the beam was characterized with a commercially available BF_3 neutron detector (N. Wood Counter Laboratory Inc., Chesterton, IN), the characteristics of which are listed in Table 2. The measured thermal neutron flux at the location of the detector modules is plotted in Fig. 13. It is 58 nv[1] at a reactor power level of 10 W, and 290 nv at 50 W. It increases linearly at higher power levels. The two modules were operated with argon/methane gas (90/10) at 1 atm, and with a cathode bias of 1150 V. In order to avoid counts from neutrons scattered from the beam cave walls, all sides of the modules, except the one facing the source, were shielded with borated aluminum. The neutron count rate recorded at a reactor power level of 50 W, and above a threshold of 30 keV, was 29 cps/cm^2 in the aluminum module, and 45 cps/cm^2 in the copper module. The resulting thermal neutron detection efficiencies are 10% (=29/290) for the aluminum module, and 16% (=45/290) for the copper module. If the straws were to be lined with ^{10}B-enriched boron carbide, the efficiency of the two modules would be 28% and 44%, respectively.

The difference in efficiency between the two detectors is probably due to a difference in the thickness of the boron carbide (B_4C) layer that lines each straw in the two modules. Fig. 14 shows the predicted efficiency of the modules as a function of the thickness of the B_4C layer. The curve peaks at around 13%, corresponding to a layer thickness of 2.5 μm. The fully developed detector will be 5 cm deep, will incorporate enriched rather than natural boron carbide, and will have an estimated efficiency of 70% based on the prototype measurements discussed above. Monte Carlo simulations show the dependence of efficiency on the thickness of the boron carbide film, as shown in Fig. 15(a). The dependence of detection efficiency on neutron energy was similarly determined and is plotted in Fig. 15(b).

Position Resolution in z Direction. The spatial resolution of the proposed detector in the direction parallel to the straw axis (z-direction) was investigated through the use of a slit collimator. Figure 16 shows the spectrum of interaction positions in each of the two meter-long modules, and in the two modules combined, with the reactor power set to 50 W. The modules were oriented as shown in Fig. 1, and placed behind a 4.5 mm thick borated aluminum collimator (^{10}B areal density of 45 mg/cm^2, 99.9% attenuation) with ten 1 mm wide slits, 10 cm apart from one another. A gas mixture of argon-methane (90-10) was employed, and all cathodes were biased to 1150 V (negative). The energy discriminator level was set to 30 keV.

The linearity of the peaks is near perfect, as illustrated in Fig. 17. The corresponding energy spectra are shown in Fig. 18, both for events under the peaks, and for background events in between peaks. The two spectra are very similar, indicating that events in between peaks are also valid neutron events, and not gamma interactions. These neutrons were either thermal neutrons that penetrated the shield avoiding absorption, or epithermal neutrons that interacted in the detector.

The mean full-width-at-half-maximum (FWHM) of all peaks in the aluminum-straw module was 7.4 mm. It was 9.1 mm in the copper module, and 9.3 mm in the combined set. The minimum values measured were 6.54 mm in the aluminum module, and 7.27 mm in the copper module. The difference observed in the two modules is probably due to the copper module's increased

[1] nv $\equiv$ neutrons/(cm^2·s)

gamma sensitivity (3 times that of the aluminum module), which affects the resolution in a manner discussed later (see section on gamma randoms).

A substantial degradation of resolution was observed at the edges of the neutron beam, which is not inherent to the detector. As the neutron beam was only 50 cm in diameter, the detector was irradiated in two steps, one covering the section from -50 cm to 0 cm, and the other covering the section from 0 cm to +50 cm. The resolution was worse towards those end points, as illustrated in Fig. 19, and deteriorated further at higher beam power levels, as shown in Figs. 20 and 21. In the experiment of Fig. 21, the detector was positioned such that an additional central section from -25 cm to +25 cm was irradiated. Clearly, the resolution degrades towards the new end points now ($\pm$25 cm), and certainly not at the center where it is actually optimal. For instance, the FWHM at the +5 cm position in the copper module is 9.23 mm when the beam irradiates the -25 cm to +25 cm section, but it is 14.4 mm (56% higher) when the beam irradiates the 0 cm to 50 cm section. Figure 22 shows the position spectra collected when the -25 cm to +25 cm section was irradiated. It is not yet understood which aspect of the irradiation is responsible for the observed degradation at the edges of the beam. The divergence of the neutron beam was too small ($\sim$3 degrees) to generate a parallax error of this magnitude.

A degradation of resolution is also observed as the detection count rate increases. This is shown both in Fig. 23 where the best resolution of each module is plotted as a function of the integral and differential count rates. The maximum rates tested were 1500 cps integral and 75 cps/mm differential. The degradation was on the order of 30% at those rates. This trend is not yet understood, but may be related to limitations in the electronic readout system. As a result, the full rate capability of the two modules was not reached.

Position Resolution in 3D. The position resolution in the two directions perpendicular to the straw axis is dictated by the straw diameter (4 mm), and the straw decoding scheme (described below). Assuming that straw decoding is 100% accurate, the position resolution in the x and y directions was identified in Monte Carlo simulations, in which random neutron interactions were distributed uniformly over the converter film of individual straws. For each interaction at point P, the coordinate of the anode P_a of the corresponding straw was recorded. The difference between the two coordinates $\Delta P = P - P_a$ was then histogramed, as shown in Fig. 24. The full width of the distribution is 4 mm in either direction. Thus, the spatial resolution of the array in either the x or y directions is 4 mm (FWHM).

In order to demonstrate the detector's position resolution in the three directions, the data collected in the experiment described above, were plotted again, this time in two-dimensional images. Figure 25 shows the two-dimensional image of the ten-slit collimator in the y-z plane (detector front face). Figure 26 shows the collimator image in the x-z plane (across the detector depth).

Additional two-dimensional images were reconstructed in similar experiments, using letter phantoms. Figure 27 shows the image created with the collimator of Fig. 28, made of acrylic letters (polymethyl methacrylate), each 9.1 mm deep and 55 mm tall, acquired at power levels of 1000-1500 W. The letters were taped onto a 1 mm thick sheet of borated aluminum, in order to lower the flux of incident neutrons, and placed 10 cm away from the detector face. Neutrons scatter within the acrylic letters at a rate of 50% before hitting the detector. The reconstructed image was adjusted for variations in straw sensitivity, and was enhanced for contrast. The image shows very good linearity, but degrades significantly in the center. This likely is a result of combined effects of beam edge degradation previously discussed, and possible effects of the plastic sleeving used in the center twisters. Whereas the presence of fittings at the two ends of each straw is required and will

not interfere if the straw ends are shielded, the central support may be eliminated or redesigned in order to minimize neutron scattering. Alternatively, the area directly in front of these fittings can be completely shielded from neutrons, thus eliminating scatter effects. It is likely that the increased power level employed for these phantoms produced an enhancement in the beam edge effects which contributed significantly to the center image blurring.

A different experiment used a phantom made of letters cut out from a thin aluminum sheet, coated with ^{10}B-enriched boron carbide ($^{10}B_4C$). The letters, which were of the same dimensions as the acrylic letters, were glued onto an aluminum backing and mounted directly onto the detector face. The image is shown in Fig. 29. The attenuation of neutrons in these letters was on the order of 10%. Again in this image, degradation in the central portion of the detector is present and some scatter from center twister insulators is evident.

Straw Decoding The ability of the detector to resolve the location of neutron interactions in the two directions normal to the straw axis is dictated by a decoding scheme that identifies the exact straw in which an event occurred. The decoding scheme differentiates signals based on their time of arrival, using delay lines. Thus, in a 5×10 straw module, a five-tap delay line identifies the row of the straw that fired, while a 10-tap delay line identifies the column.

Figure 30 shows the time spectra of neutron interaction events under uniform irradiation conditions. Events are grouped into 10 peaks in the upper panel, corresponding to the ten columns in the array. The same events are grouped under five peaks in the lower panel, corresponding to the five rows in the array. Once the detector is calibrated using these results, the x and y coordinates of any event are determined by identifying the row and column of the straw in which the event occurred.

Straw decoding using signal timing works well along most of the length of the straw module, but is limited at the very end of the detector due to cross-talk. Figure 31 shows the correlation between the time of arrival of signals, and the corresponding location of interaction events. Most events are clearly grouped in narrow bands, except for the left end of the detector, where the bands merge. A similar plot of the timing of signals in the direction of the module rows was constructed and is shown in Fig. 32. The separation between the five rows is clear, except at the extreme right end.

In addition to identifying the location of interactions in the x and y directions, as required for position resolution (see previous section), straw decoding was used to determine the response of individual straws within the array, under uniform irradiation. Events were recorded separately for each straw, using the readout scheme outlined above. Figure 33 shows a cross-sectional view of the two straw modules in the $x - y$ plane that is color-graded according the number of events recorded in each straw. The resulting map indicates the presence of several non-functional straws (black), and only slight variations in sensitivity between straws, within each of the modules. The copper-straw module is more sensitive than the aluminum-straw module due to a thicker boron carbide coating (see Fig. 15a). The corresponding two-dimensional image is shown in Fig. 34.

Gamma Efficiency & Discrimination The response of the copper straw module to gamma radiation was determined in the following experiment. A 246 μCi ^{137}Cs source was placed 25 cm away from the face of the module. The gamma fluence Φ through the detector module was estimated using the relation $\Phi = N/(4\pi d^2)$, where N is the number of photons emitted by the source (94% at 662 keV), and d is the distance between the source and the detector. The average fluence through the detector was 500 photons/(cm^2·s), or 200,000 photons/s over its face area (400 cm^2). The number of photons counted above a threshold of 30 keV, was 0.0607 cps. The resulting gamma

detection efficiency is 3.0×10^{-7} (=0.0607/200,000). The gamma discrimination factor, defined as the ratio between the neutron and gamma efficiencies, is 0.93×10^{6} (=$0.28/3.0\times10^{-7}$).

Gamma Randoms Random events due to gamma interactions in the detector, that may affect the position resolution of neutron events, were investigated in Monte Carlo simulations. These are events that coincide in time with valid neutron events, and should not be confused with isolated gamma interactions, which are successfully discriminated with the energy threshold, as discussed above. The simulation assumed a module of 50 straws, each made of a 50 μm thick copper wall, 4 mm in diameter, and 100 cm in length. The module was irradiated uniformly from the side (4×100 cm^2 sensitive area) with 1.33 MeV photons (assuming this energy as the average energy of gammas present in the neutron beam). The predicted sensitivity is 4.5×10^{6} (gammas/s)/(rad/h). The gamma dose present in the neutron beam was measured at the location of the detector, using a nitrogen-filled ionization chamber (LND 50317), the specifications of which appear in Table 3. The gamma dose, plotted in Fig. 35, was 5.5 rad/hr at a reactor power level of 100 kW, and increased linearly at higher power levels.

Based on these values, and the sensitivity estimate discussed above, Table 4 was constructed, listing the rate of gammas depositing some charge in the detector, and the rate of gamma events that arrive on top of neutron events (gamma randoms) within the 300 ns window of the charge-integrating ADC. Such randoms can cause degradation of spatial resolution even though the gamma pulse height is well below the detection threshold. Even at the lowest reactor power levels, the probability of gamma randoms is almost 100%.

Prototype Performance Summary Table 5 summarizes the measured performance of the prototype detector.

Full Design Projections The Small Angle Neutron Scattering (SANS) instrument station, scheduled for completion at the Spallation Neutron Source facility in 2006, is one of the instruments that requires neutron detectors with a large sensitive area, high spatial resolution and the ability to deal with high count rates. We propose a detector made up of 58 modules similar to the prototype tested, that will have a sensitive area of 1 m^2, and will satisfy the SANS requirements, shown in Table 6.

We estimate that the cost of the electronic readout system required for the 1 m^2 detector is under \$100,000. The readout system will include 16 ADC units (\$3550 ea.), four gigabit-data-interface units (\$2000 ea.), four computers (\$3000 ea.), and two trigger units (\$7200 ea.). Each ADC unit is capable of reading out 4 detector modules, and four ADC units interface with one data interface (DI) unit. The maximum rate supported by each DI is 5 MHz, thus the maximum count rate supported in each detector module will be 330,000 cps. The combined 58 modules will thus support rates up to 2×10^{7} cps.

2 Publications

Certain aspects of the detector development were presented and published in the record of the IEEE Nuclear Science Symposium held in Norfolk, VA, on November 10-16, 2002.

J. L. Lacy, A. Athanasiades, N. N. Shehad, R. A. Austin and C. S. Martin, Novel neutron detector for high rate imaging applications, *2002 IEEE Nuclear Science Symposium Conference Record,* 2002.

References

[1] R. Cooper, I. Anderson, C. Britton, K. Crawford, L. Crow, P. DeLurgio, C. Hoffmann, D. Hutchinson, R. Klann, I. Naday, and G. Smith. A program for neutron detector research and development: A white paper based on a workshop held at Oak Ridge National Laboratory. March 2003. http://www.sns.gov/documentation/pubs.htm.

Table 1: Description of Experiments at TAMU NSC.

experiment	reactor power	integral count rate		differential count rate		Collimator
		Al	**Cu**	**Al**	**Cu**	
	(W)	(cps)	(cps)	(cps/mm)	(cps/mm)	
1	50	82	150	4.9	7.6	10-slit
2	100	166	303	9.9	15	10-slit
3	500	812	1482	49	75	10-slit
4	50	3816	5940			B_4C-coated letters
5	50	3818	6121			- no collimator -
6	100	8297	12765			- no collimator -
7	1000	6385	9642			acrylic letters
8	1500	9547	14120			acrylic letters

Table 2: N. Wood Model G-5-1 BF_3 neutron detector manufacturer specifications.

gas pressure (Torr)	600
effective length (mm)	24
effective diameter (mm)	16
thermal neutron sensitivity (cps/nv^2)	0.25

Table 3: LND 50317 ionization counter manufacturer specifications.

fill gas	Nitrogen
fill pressure (Torr)	100
effective length (mm)	143
maximum diameter (mm)	50.8
gamma sensitivity, ^{60}Co [A/(rad/hr)]	1.8×10^{-12}

Table 4: Estimate of gamma random events in the copper straw module, during experiments at TAMU NSC.

reactor power (kW)	gamma dose† (rad/h)	gamma rate‡ (10^6 gammas/s)	gamma randoms¶ (%)
0.050	3.39*	15	98
0.100	3.39*	15	98
0.500	3.40*	15	98
100	5.5	25	100
250	8.8	40	100
500	14	63	100
1000	25	113	100

† Measured at the location of the detector during experiments, except as indicated.

‡ Using gamma sensitivity estimate of 4.5×10^6 (gammas/s)/(rad/hr), obtained in Monte Carlo simulations.

¶ Probability that a gamma event will coincide with a neutron event, within a time window of 300 ns.

* Extrapolated from the values of Fig. 35 at power levels of 100, 250, 500 and 1000 kW.

Table 5: Properties and performance of two prototype modules tested at TAMU NSC.

	aluminum straws	copper straws
dimensions	100×1.73×4 cm^3	100×1.73×4 cm^3
number of straws	50	50
number of modules	1	1
neutron detection efficiency (thermal)	10%	16%
position resolution	7×4×4 mm^3	9×4×4 mm^3
max count rate tested	9547 cps	14120 cps
max pixel count rate tested	49 cps/mm	75 cps/mm
timing resolution	25 ns	25 ns
gamma efficiency		3×10^{-7}

Table 6: Properties and performance of proposed detector, and requirements for Small Angle Neutron Scattering (SANS) instrument at SNS (Oakridge).

	proposed design	SANS requirements [1]
dimensions	$100\times100\times4$ cm^3	100×100 cm^2
number of modules	58	-
neutron detection efficiency (80 meV)	50%	50%
position resolution	$7\times4\times4$ mm^3	5×5 mm^2
count rate (overall)	2×10^7 cps	2×10^7 cps
pixel count rate		1500 cps
gamma efficiency	10^{-7}	10^{-7}

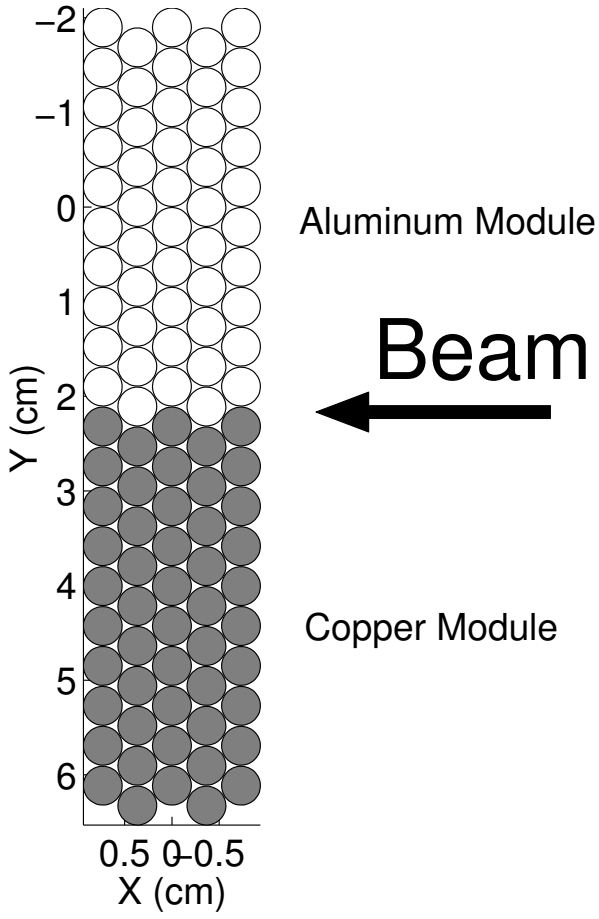

Figure 1: Schematic drawing of the two prototype modules, in the orientation used during testing.

Figure 2: Prototype detector modules.

Figure 3: Prototype detector and housing.

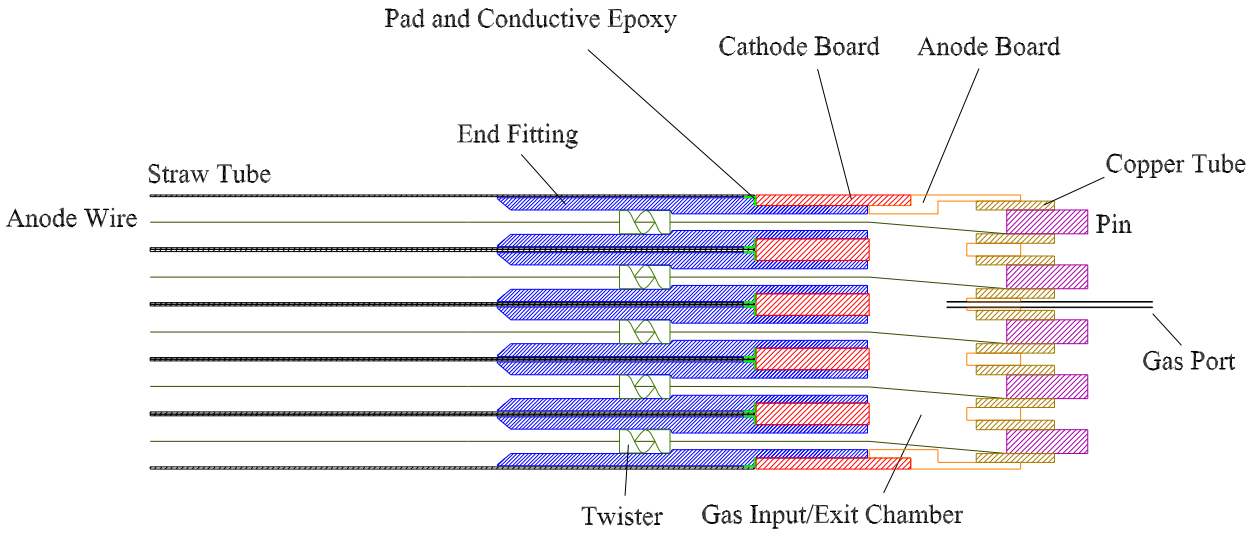

Figure 4: Schematic drawing of the end board assembly.

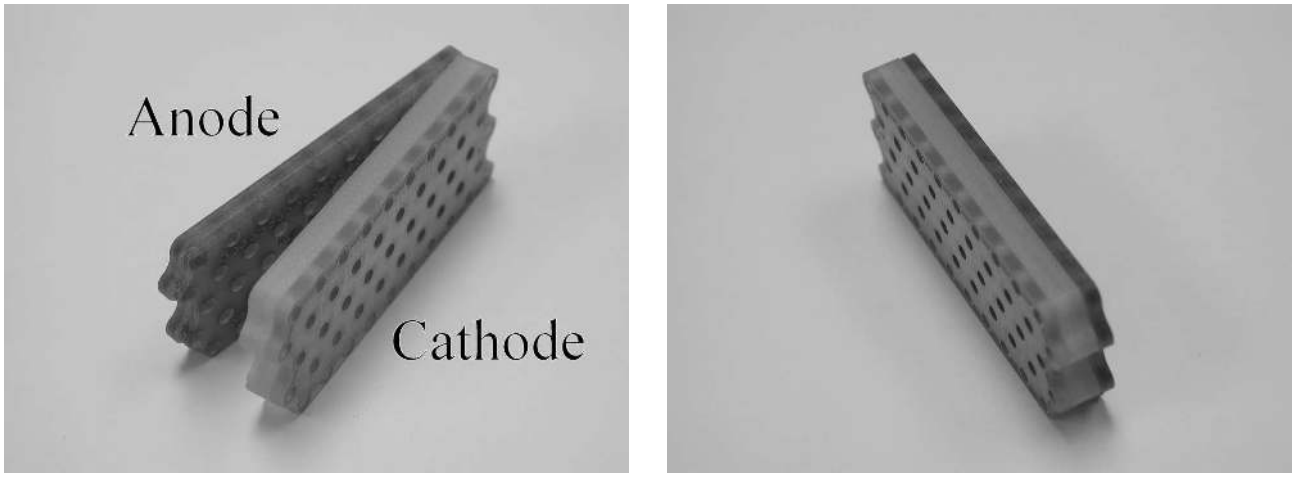

(a) (b)

Figure 5: (a) Anode and cathode board separately, (b) Anode and cathode boards mated together forming a gas-tight cavity.

Figure 6: Fixture used for wiring straw detectors located in a class 100 clean room.

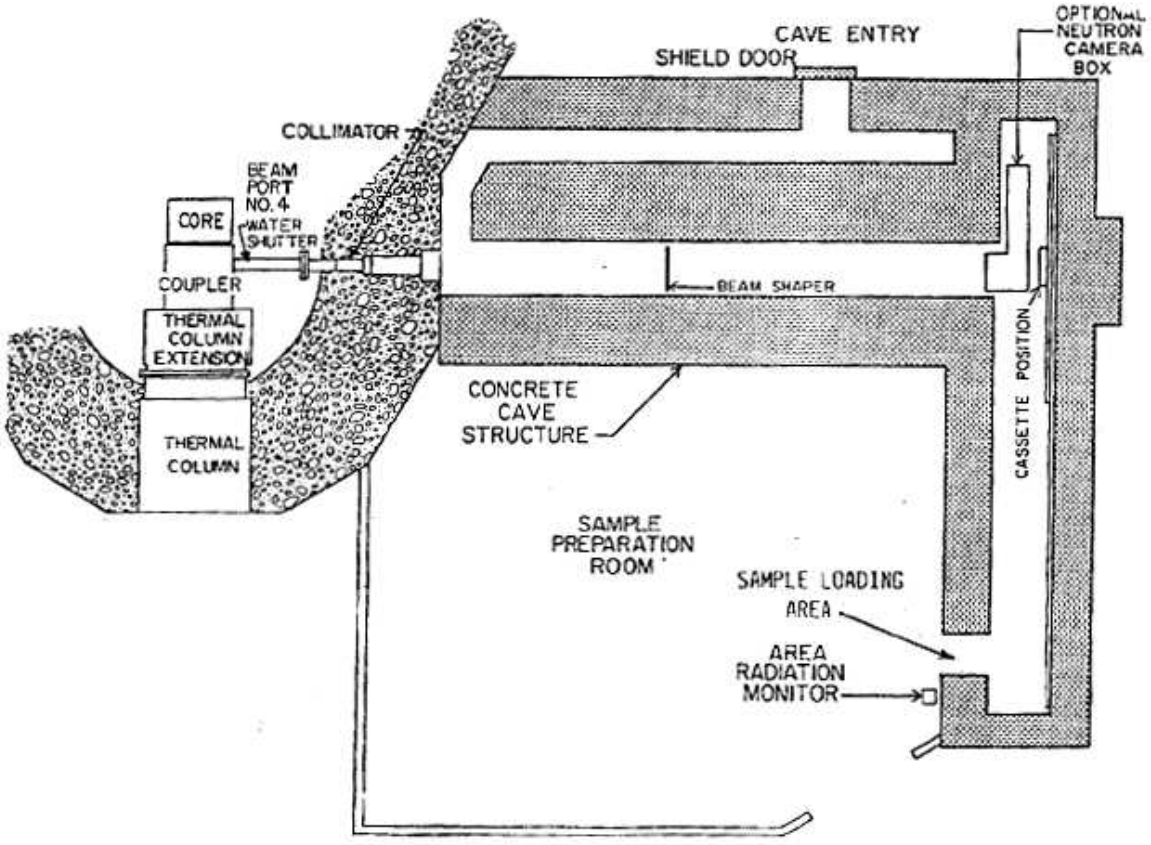

Figure 7: Schematic of beam port area used for prototype testing at the Texas A&M University Nuclear Science Center.

Figure 8: The prototype detector shown as it is lowered inside the cave that contains the neutron beam. A collimator with the letters "PROPORTIONAL TECH." is attached on the front face of the detector.

Figure 9: Instruments used during prototype testing at TAMU NSC.

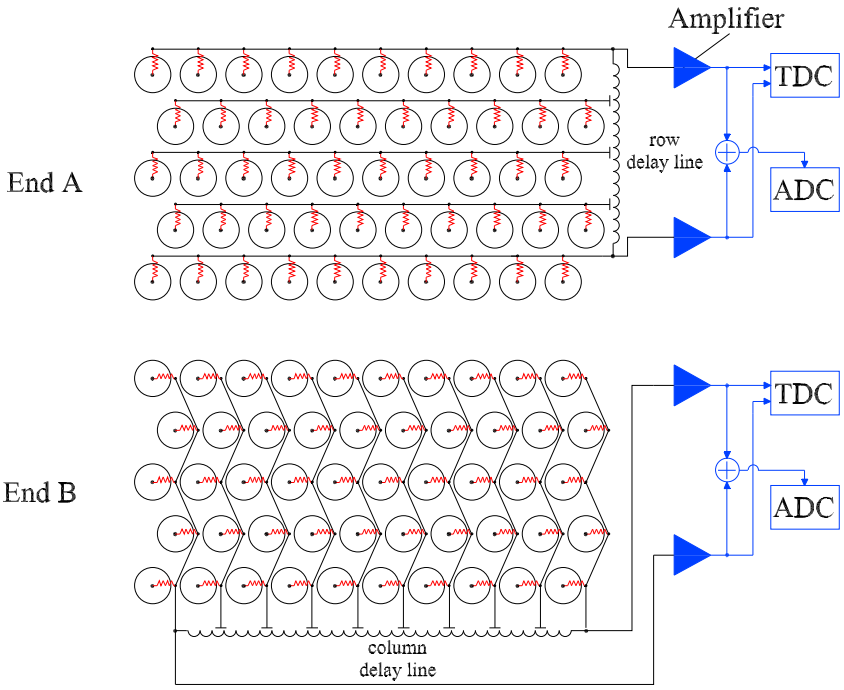

Figure 10: Electronics setup for straw readout, showing circuitry connected to the two respective ends of each module.

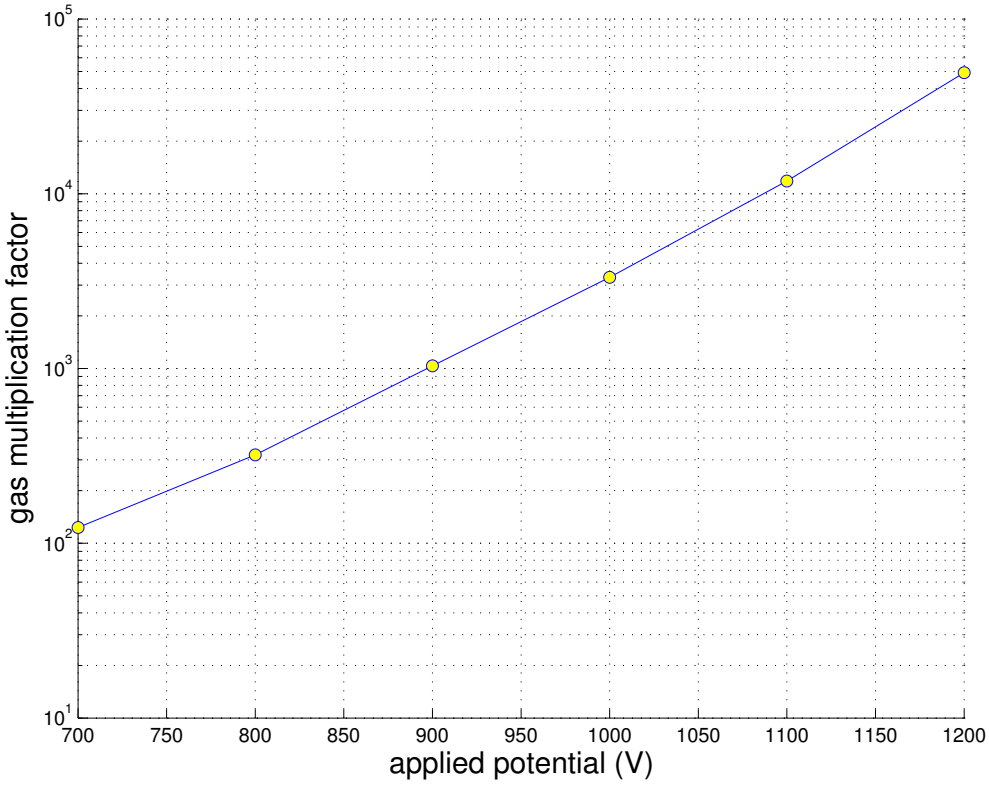

Figure 11: Gas amplification factor in the prototype detector, filled with 90% argon, 10% methane at 1 atm, as a function of detector bias voltage.

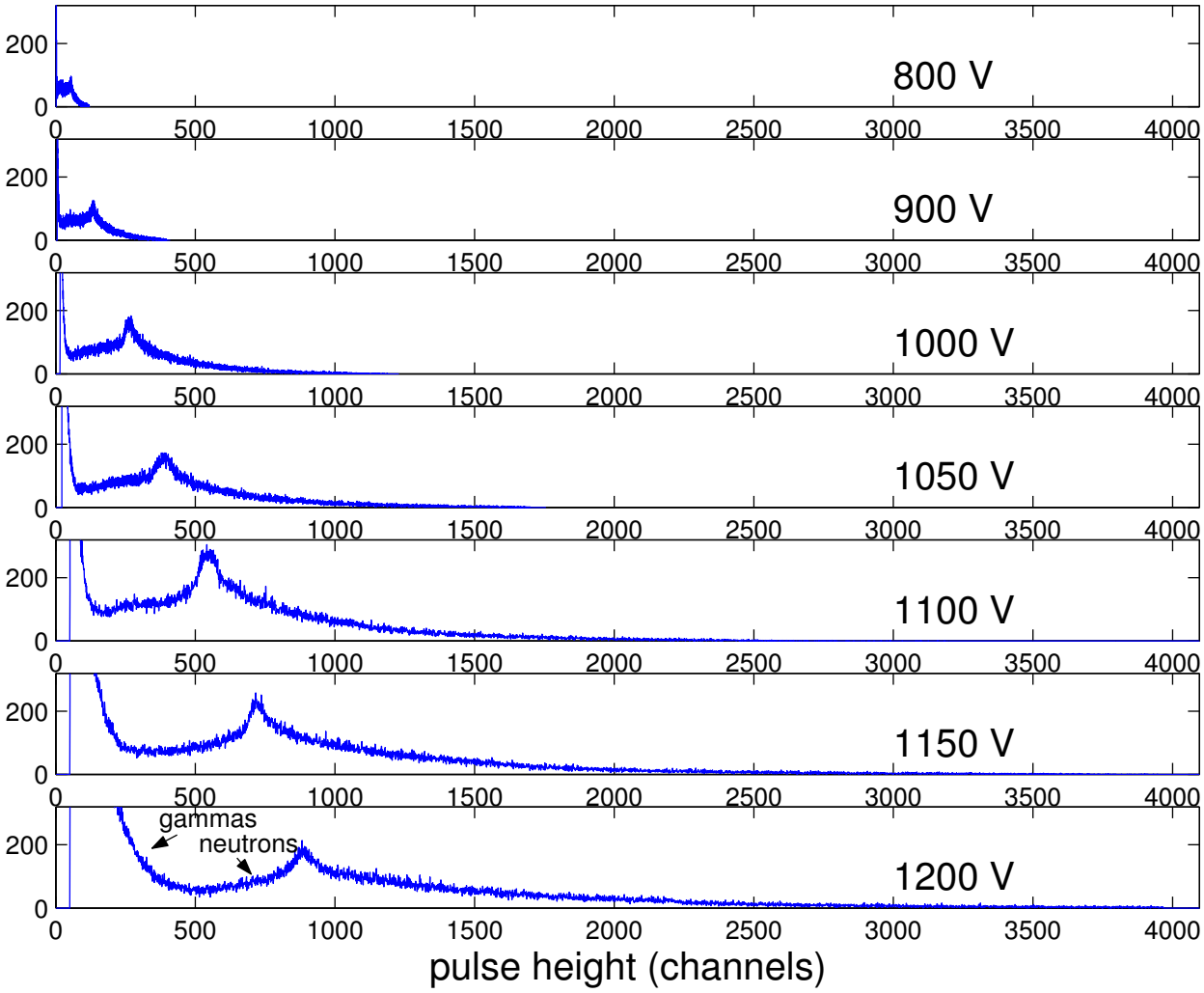

Figure 12: Energy spectra collected in the prototype detector from a moderated ^{252}Cf source. The detector cathode was biased to the voltage indicated in each panel. The gas mixture was argon-methane (90-10).

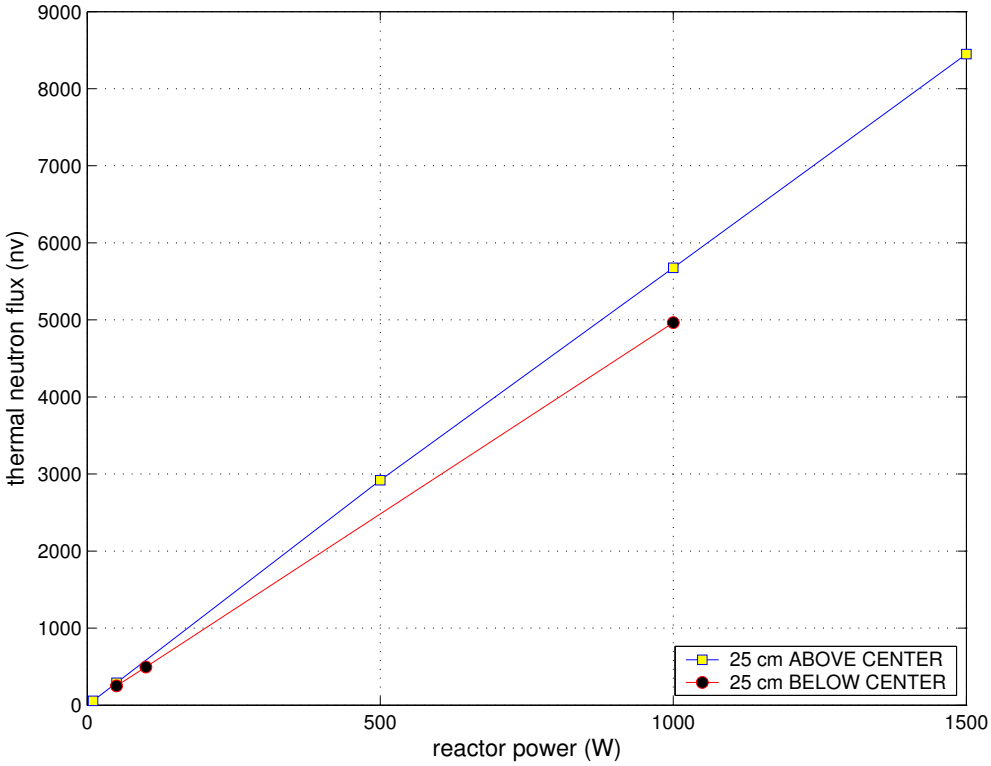

Figure 13: Thermal neutron flux measured at the location of the prototype detector, during testing at TAMU NSC beam port 4. Measurements were taken 25 cm above and below the beam center.

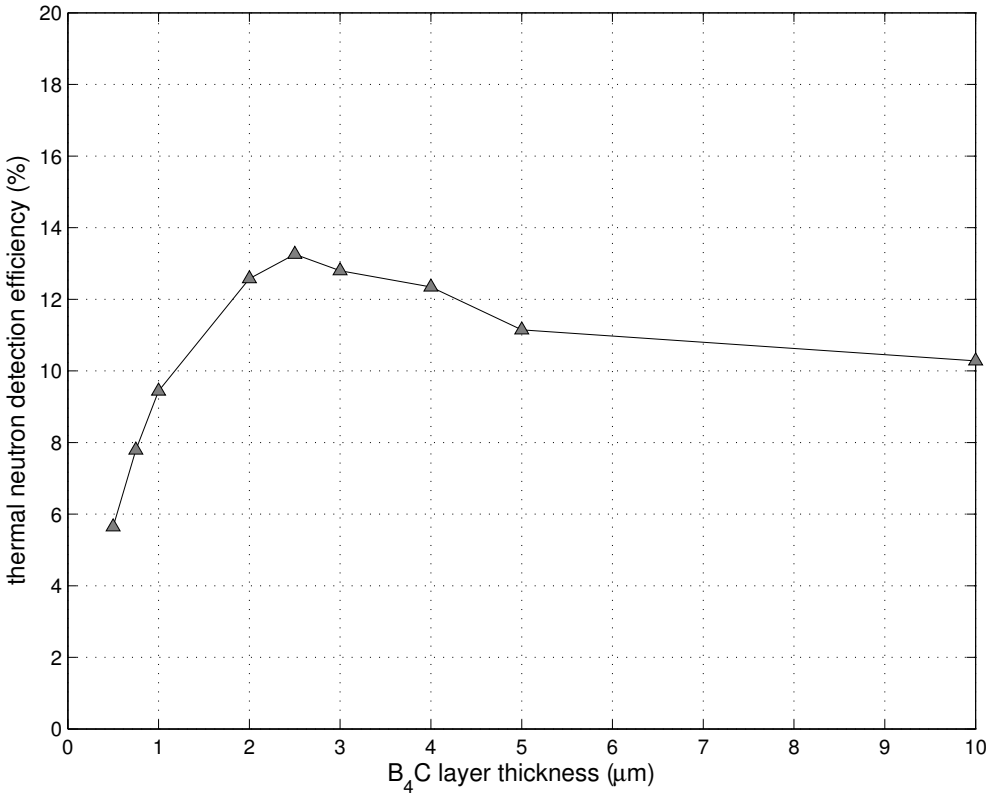

Figure 14: Predicted thermal neutron detection efficiency of a 1.73 cm deep array of unenriched B_4C-lined straws (4 mm in diameter), at various film thicknesses.

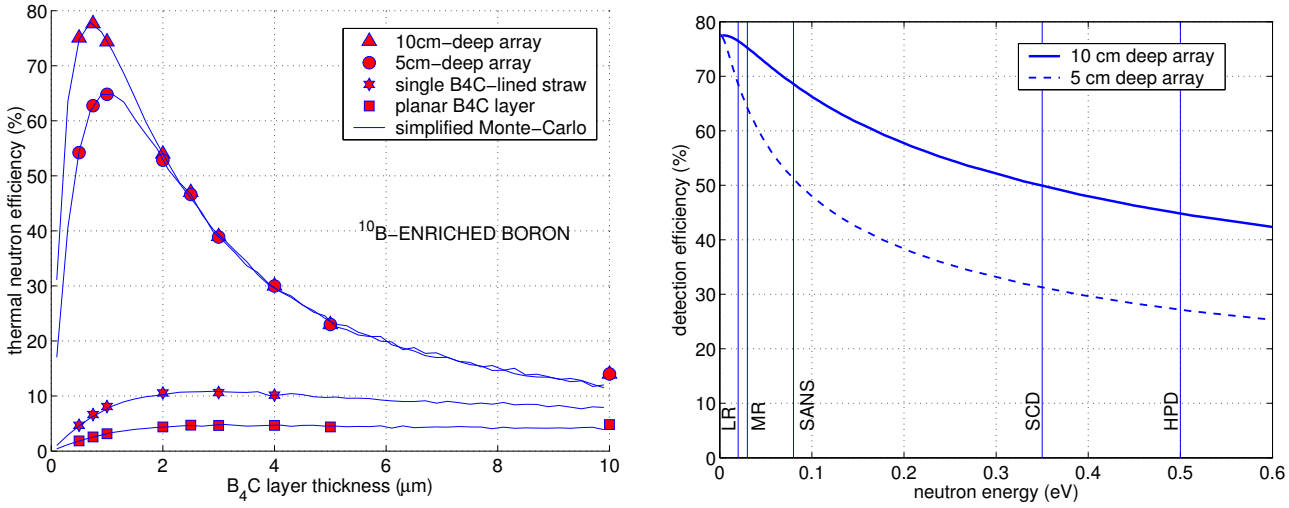

(a) (b)

Figure 15: (a) Predicted thermal neutron detection efficiency of a single ^{10}B-enriched B_4C-lined straw tube (4 mm in diameter), and of arrays of such detectors, at various film thicknesses. Results for a planar film of ^{10}B-enriched B_4C are included for comparison. (b) Detection efficiency as a function of neutron energy for two array depths, and with a B_4C thickness of 1 μm. The SNS small angle neutron scattering instrument (SANS) efficiency requirement of >50% at 80 meV is indicated by the vertical line, and is readily met with a 5 cm deep array. The other reference lines indicate the energy requirements (at 50% efficiency) of other instruments at SNS. LR: Liquids Reflectometer; MR: Magnetism Reflectometer; SCD: Single-Crystal Diffractometer; HPD: High-Pressure Diffractometer.

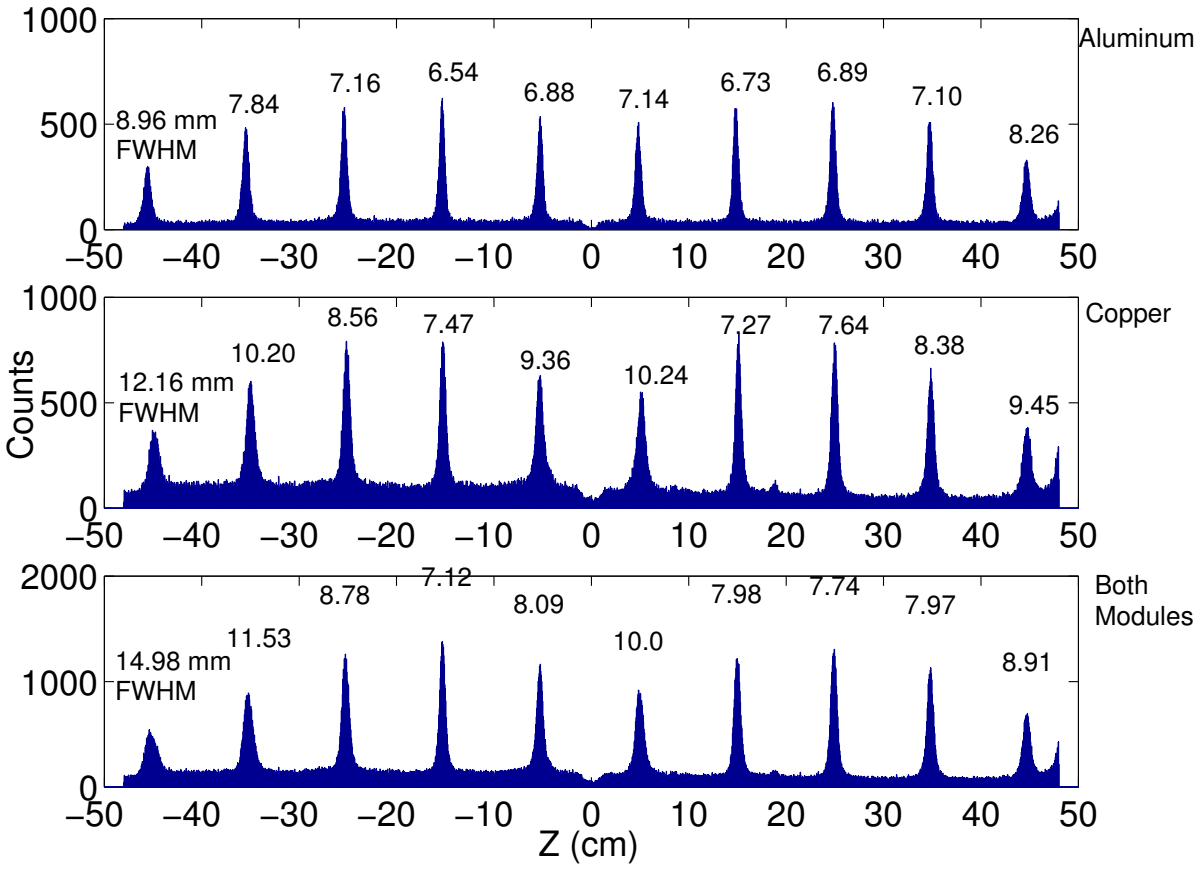

Figure 16: Position spectra in the direction along the straw axis (z direction), collected in the prototype detector, using a collimator, and at a reactor power level of 50 W. The detector was operated with an argon-methane gas flow, at 1150 V. The full-width-at-half maximum (FWHM) is indicated above each peak. The absence of counts at 0 cm is due to the presence of a fitting that supports the anode wire at the center of each meter-long straw.

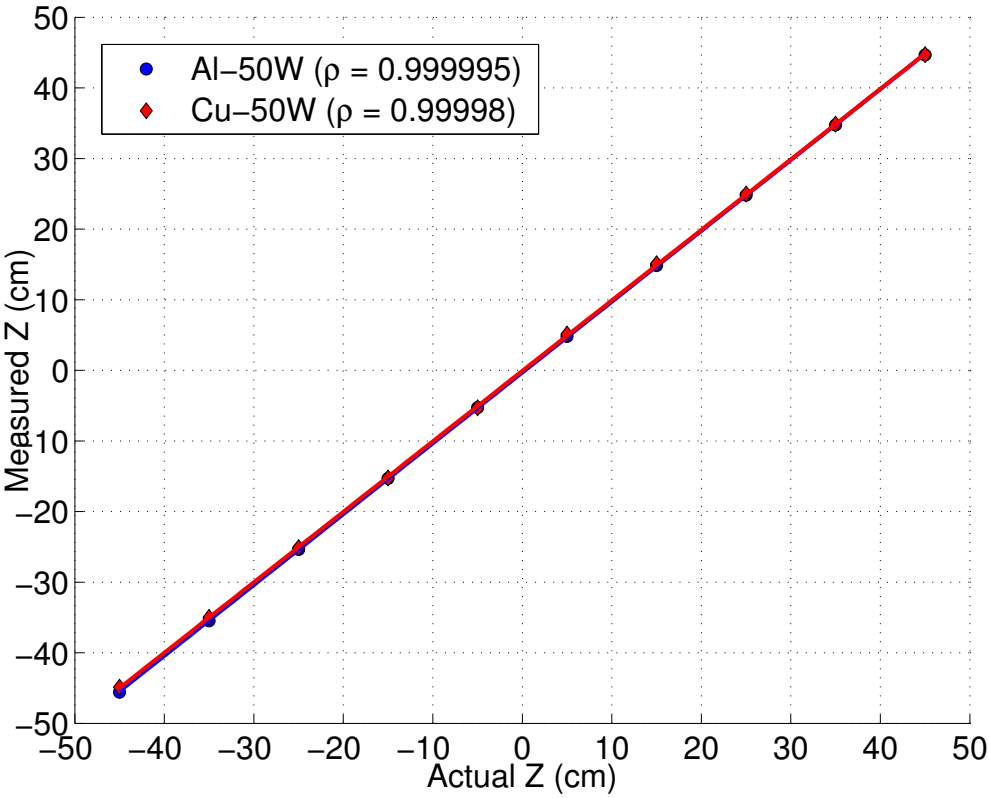

Figure 17: Position linearity of the individual peaks shown in Fig. 16.

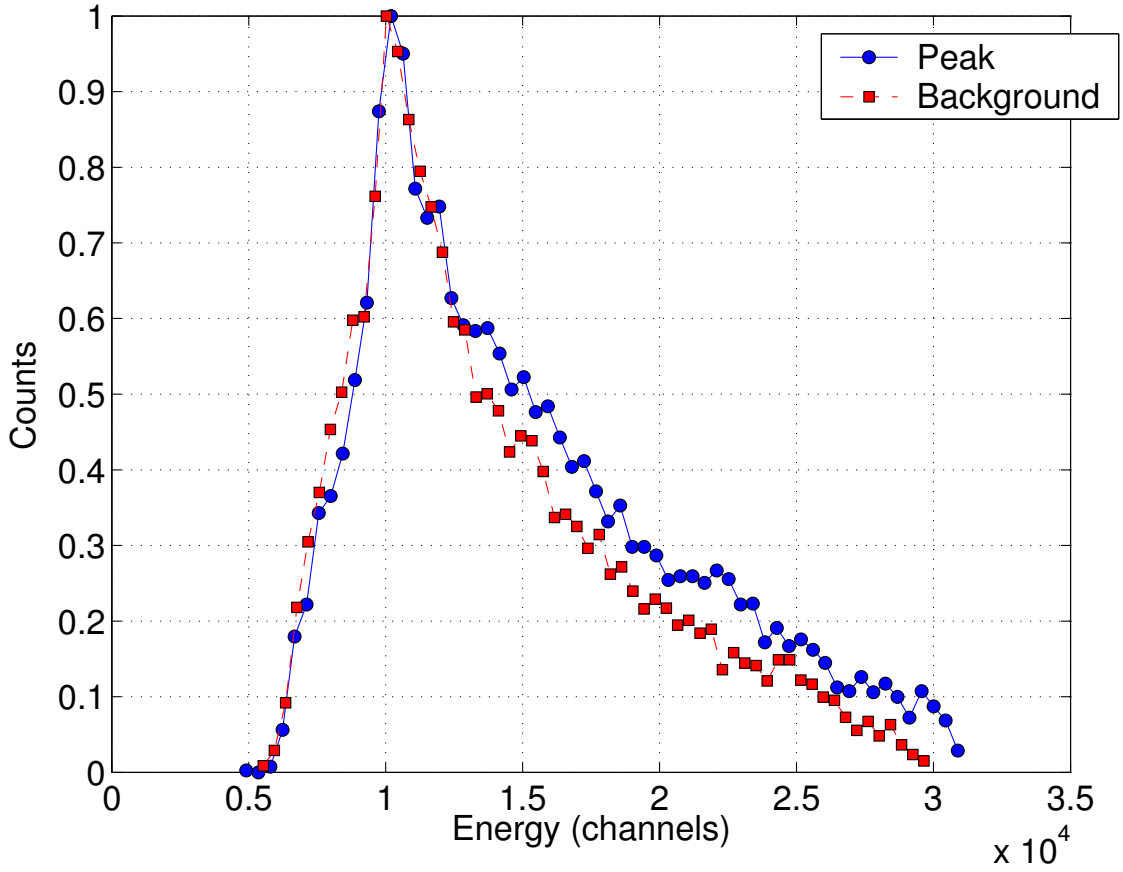

Figure 18: Energy spectra of events under the peaks of Fig. 16, and in between peaks (background).

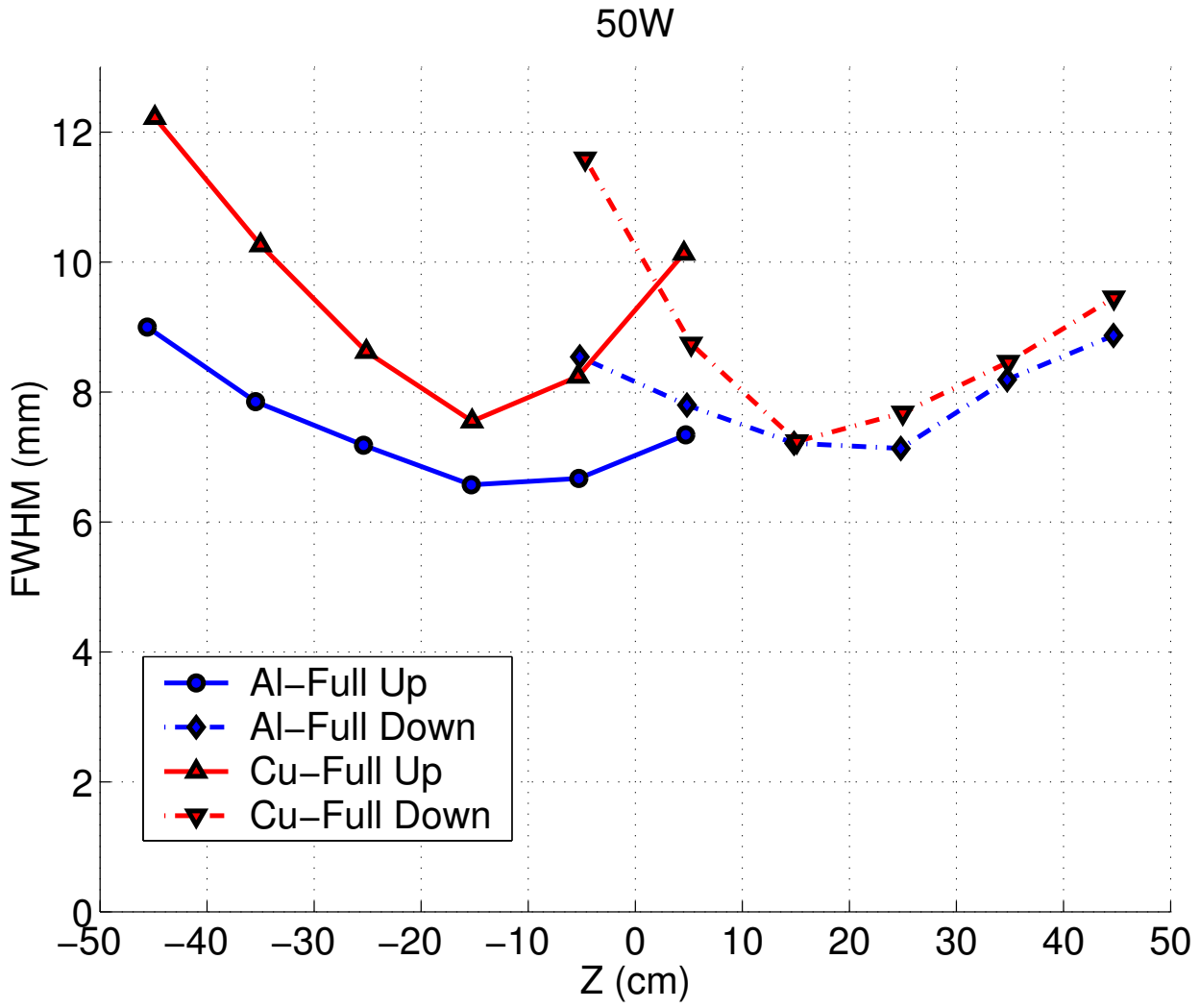

Figure 19: Spatial resolution (FWHM) along the length of each of the two modules tested (Al-aluminum, Cu-copper). Data were collected at a reactor power level of 50 W. Due to the limited beam size, the detector had to be moved to two different positions (Full Up, Full Down) in order to ensure full coverage. As a result, its two halves (-50 cm to 0 cm, and 0 cm to +50 cm) were irradiated separately.

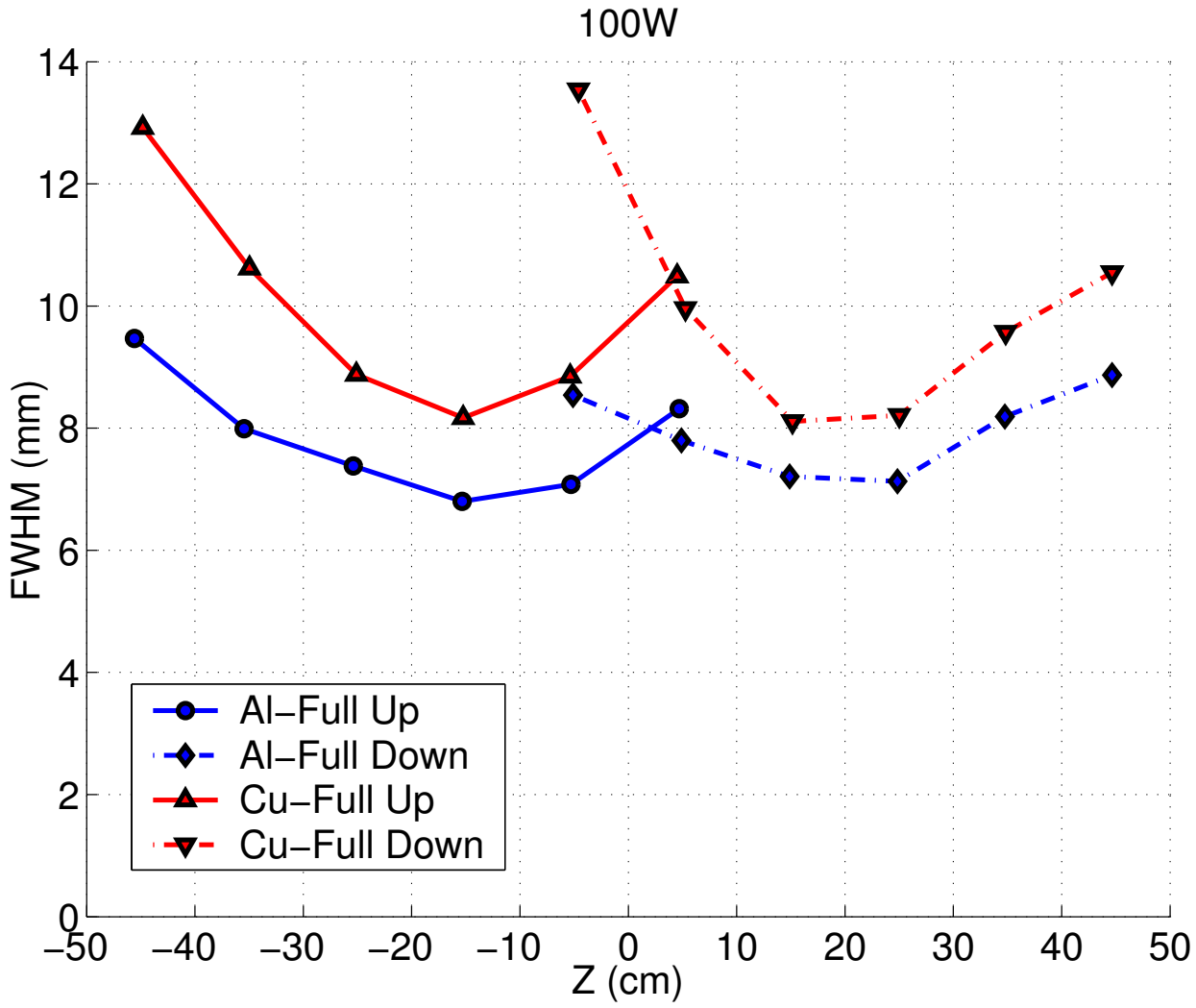

Figure 20: Spatial resolution (FWHM) along the length of each of the two modules tested (Al-aluminum, Cu-copper). Data were collected at a reactor power level of 100 W. Due to the limited beam size, the detector had to be moved to two different positions (Full Up, Full Down) in order to ensure full coverage. As a result, its two halves (-50 cm to 0 cm, and 0 cm to +50 cm) were irradiated separately.

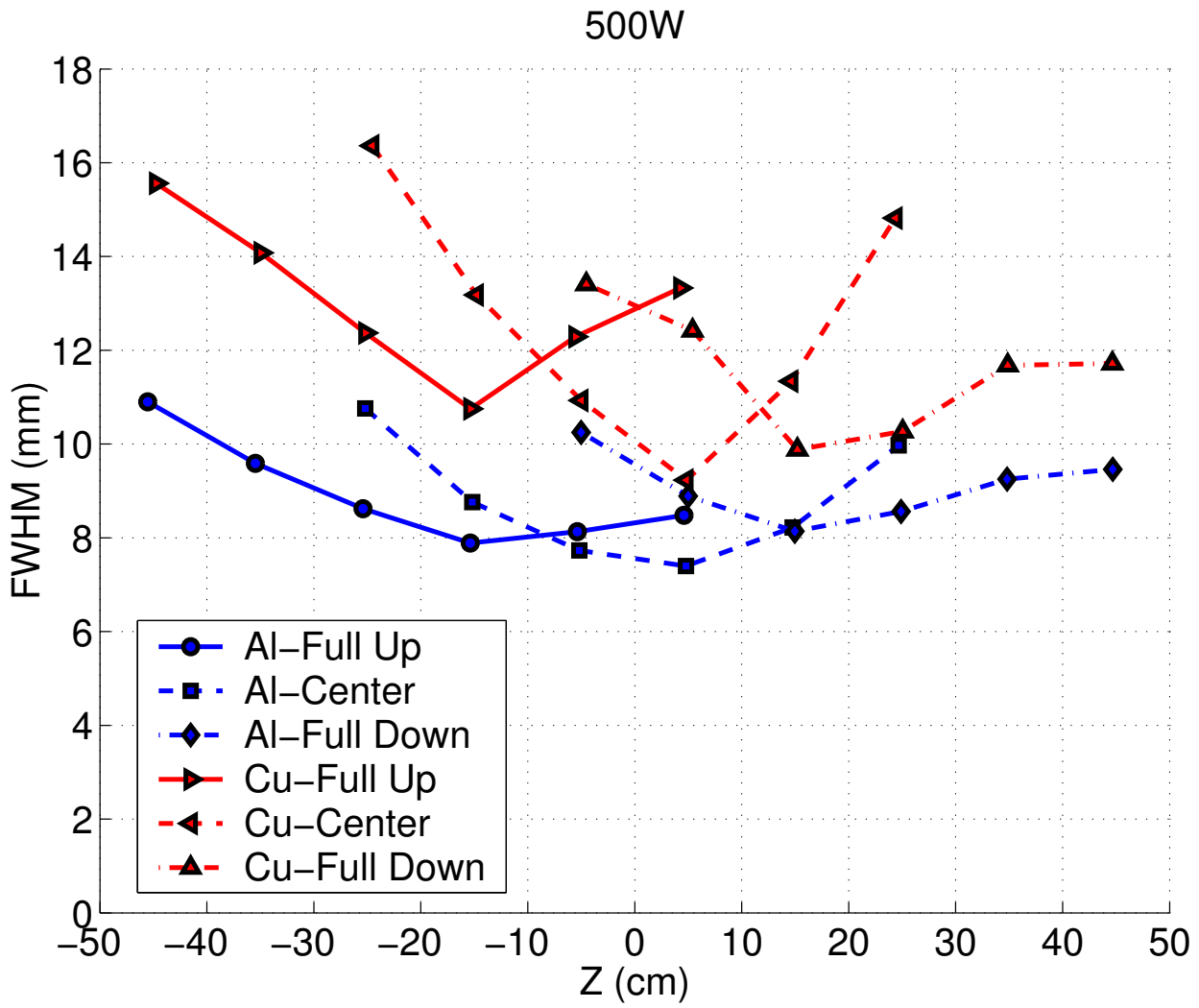

Figure 21: Spatial resolution (FWHM) along the length of each of the two modules tested (Al-aluminum, Cu-copper). Data were collected at a reactor power level of 500 W. Due to the limited beam size, the detector had to be moved to two different positions (Full Up, Full Down) in order to ensure full coverage. As a result, its two halves (-50 cm to 0 cm, and 0 cm to +50 cm) were irradiated separately. A third section (Center) from -25 cm to +25cm was irradiated as well.

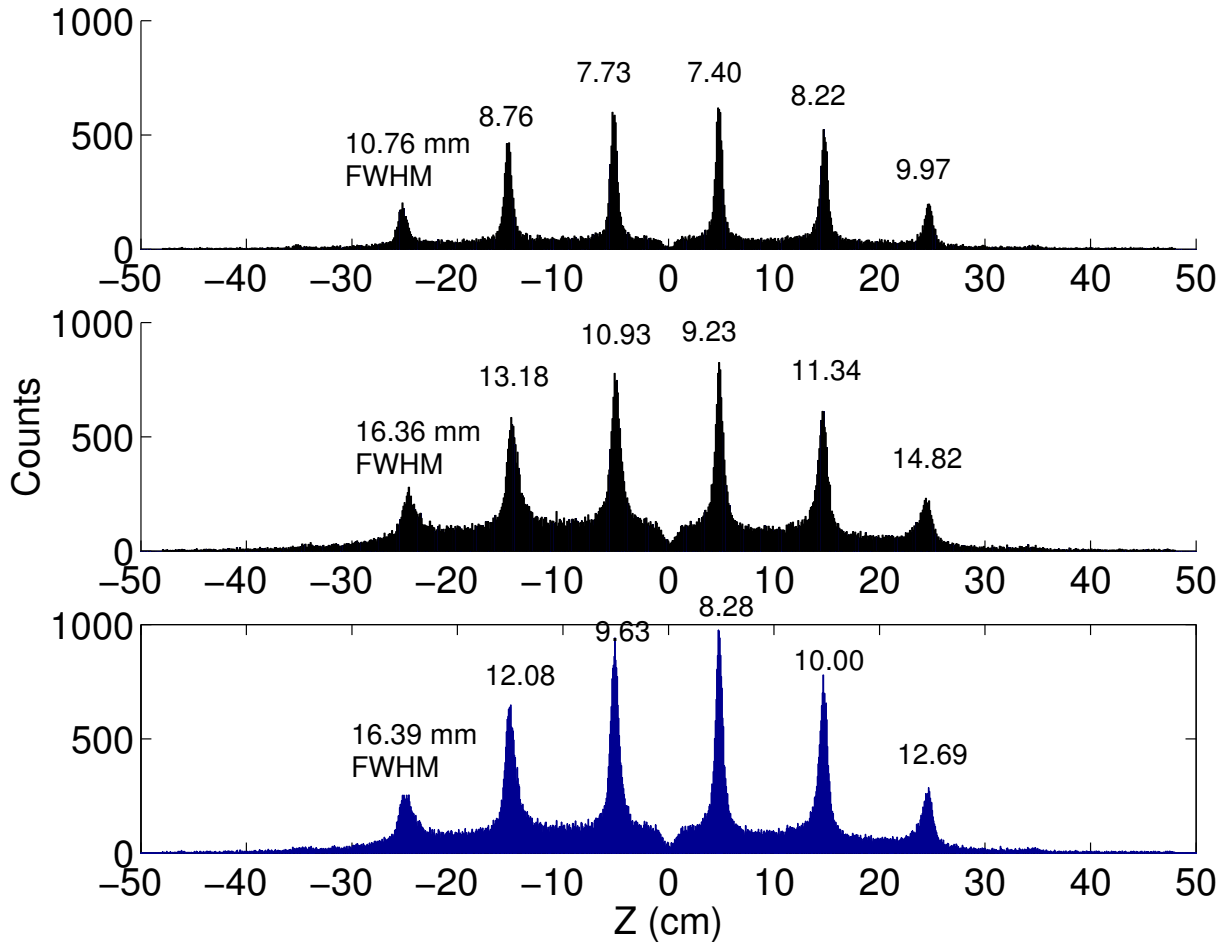

Figure 22: Position spectra in the direction along the straw axis (z direction), collected in the prototype detector, using a collimator, and at a reactor power level of 500 W. The detector was operated with an argon-methane gas flow, at 1150 V. The full-width-at-half maximum (FWHM) is indicated above each peak. The absence of counts at 0 cm is due to the presence of a fitting that supports the anode wire at the center of each meter-long straw.

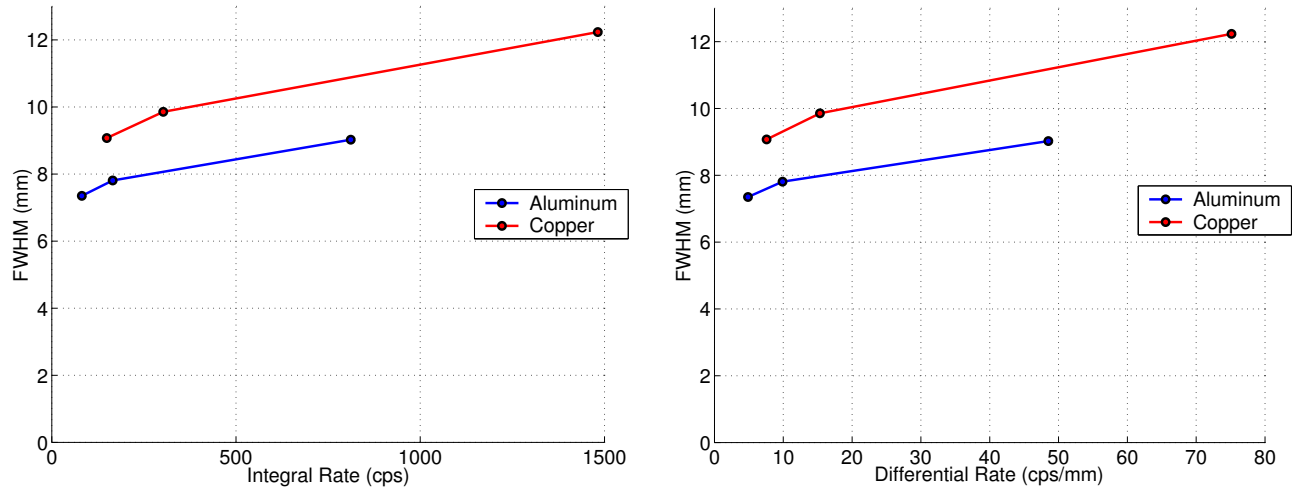

(a) (b)

Figure 23: (a) Spatial resolution as a function of the integral count rate in the prototype detector. The three different rates correspond to reactor power levels of 50 W, 100 W and 500 W. (b) Spatial resolution as a function of the differential count rate (along the straw length).

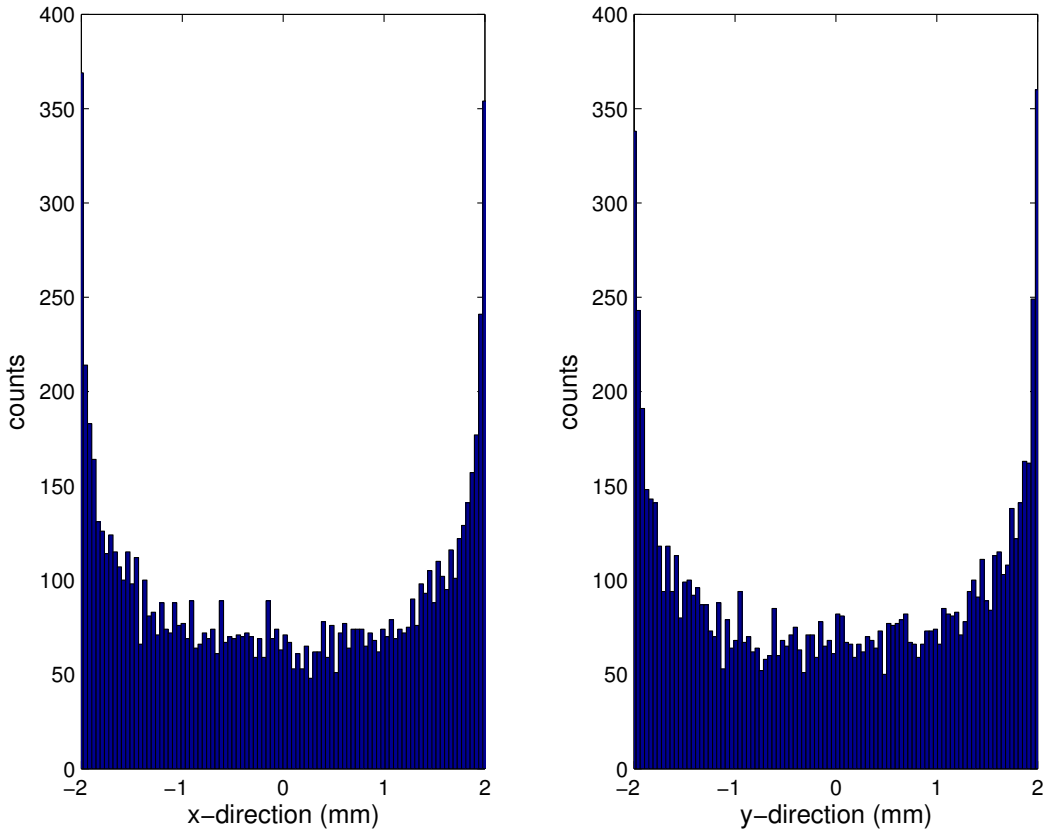

Figure 24: Distribution of spatial error in the x-direction (*left*), and the y-direction (*right*), as determined in Monte Carlo simulations.

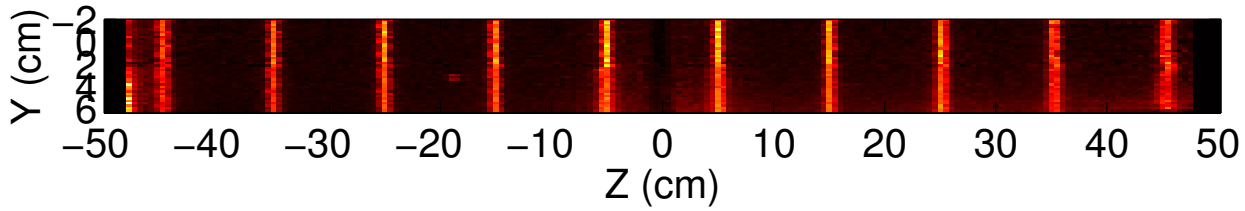

Figure 25: Two-dimensional image of ten-slit collimator, in the plane parallel to the detector face (yz plane). The neutron beam was in the positive x-direction (normal to the page).

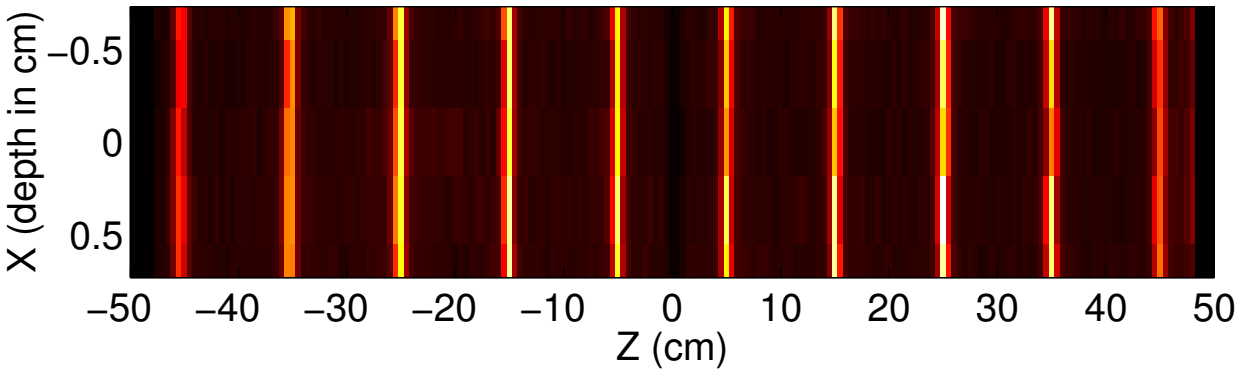

Figure 26: Two-dimensional image of ten-slit collimator, in the plane normal to the detector face (xz plane). The neutron beam was in the positive x-direction.

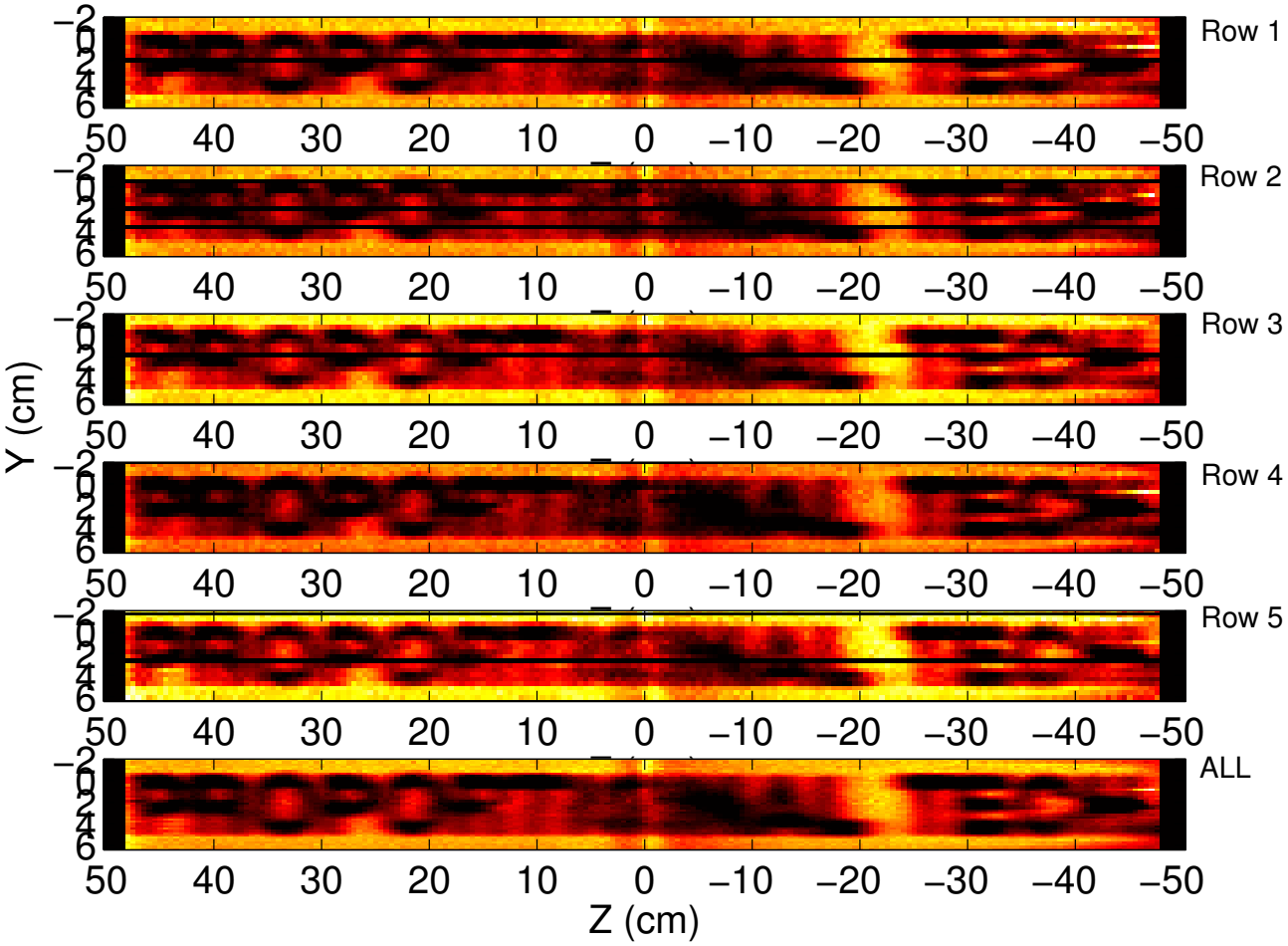

Figure 27: Two-dimensional image created in the prototype detector, using the collimator of Fig. 28. Separate images are shown for each row in the detector (group of 10 straws), and for all rows combined. Row 1 is the row on the front face of the detector.

Figure 28: Acrylic letter collimator.

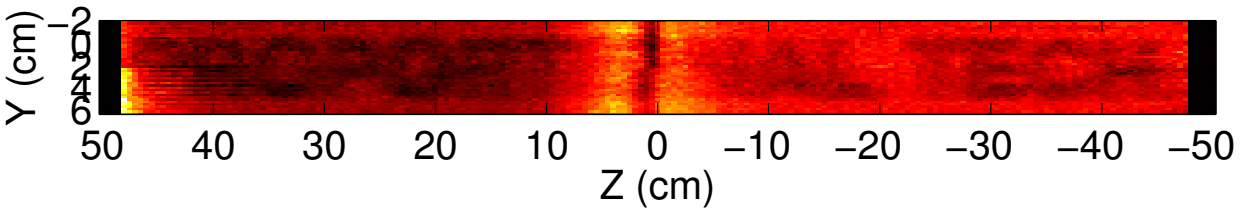

Figure 29: Two-dimensional image created in the prototype detector, using a collimator with $^{10}B_4C$-coated aluminum sheet letters.

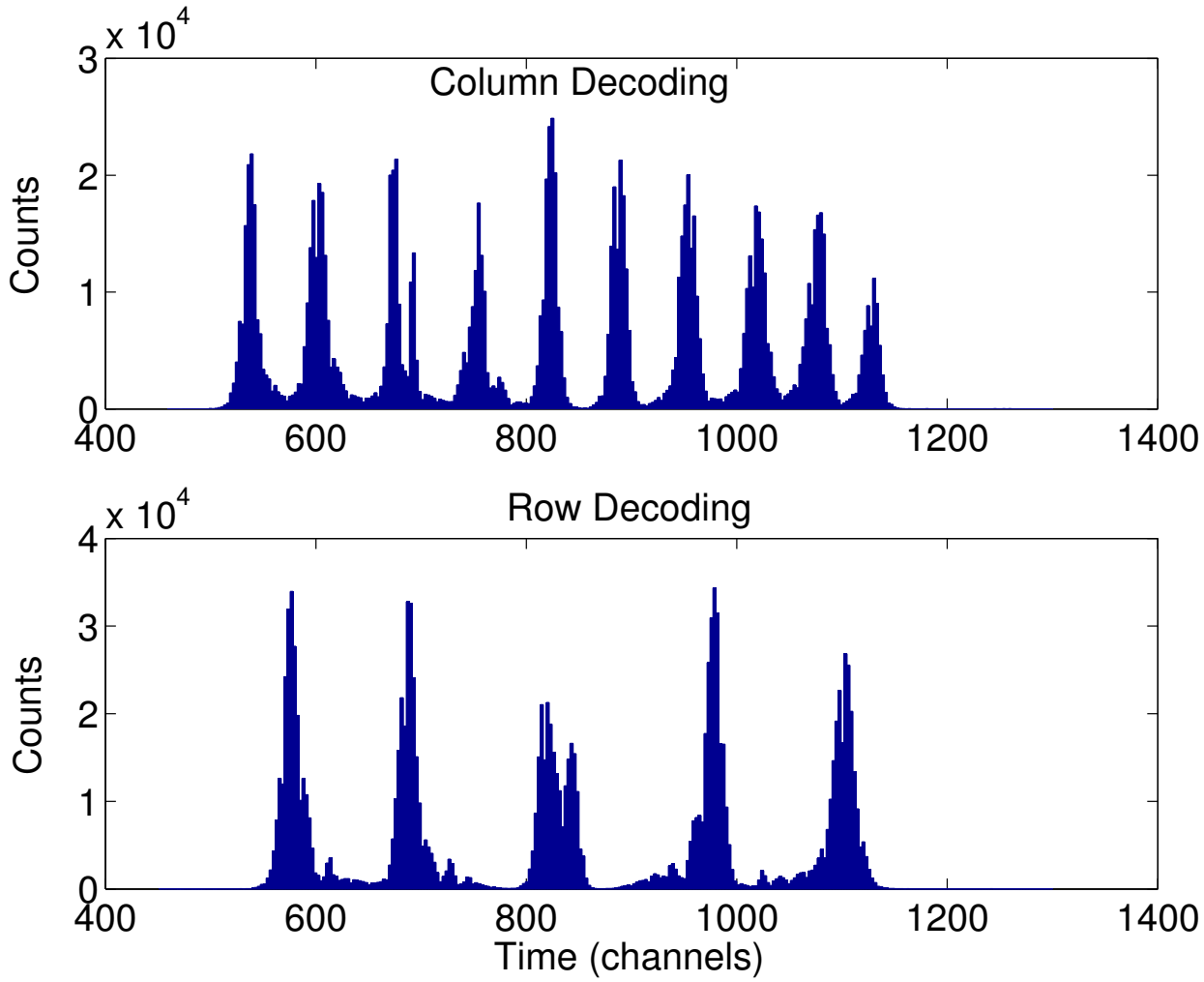

Figure 30: Time delay spectra of neutron interaction signals in the prototype detector. The readout scheme for straw decoding uses delay lines that group all events into 10 columns and 5 rows (for a 10×5 array), according to the timing of the signals. Each of the ten peaks in the upper panel corresponds to a different column of straws in the detector. Similarly, each of the five peaks in the lower panel corresponds to a different row.

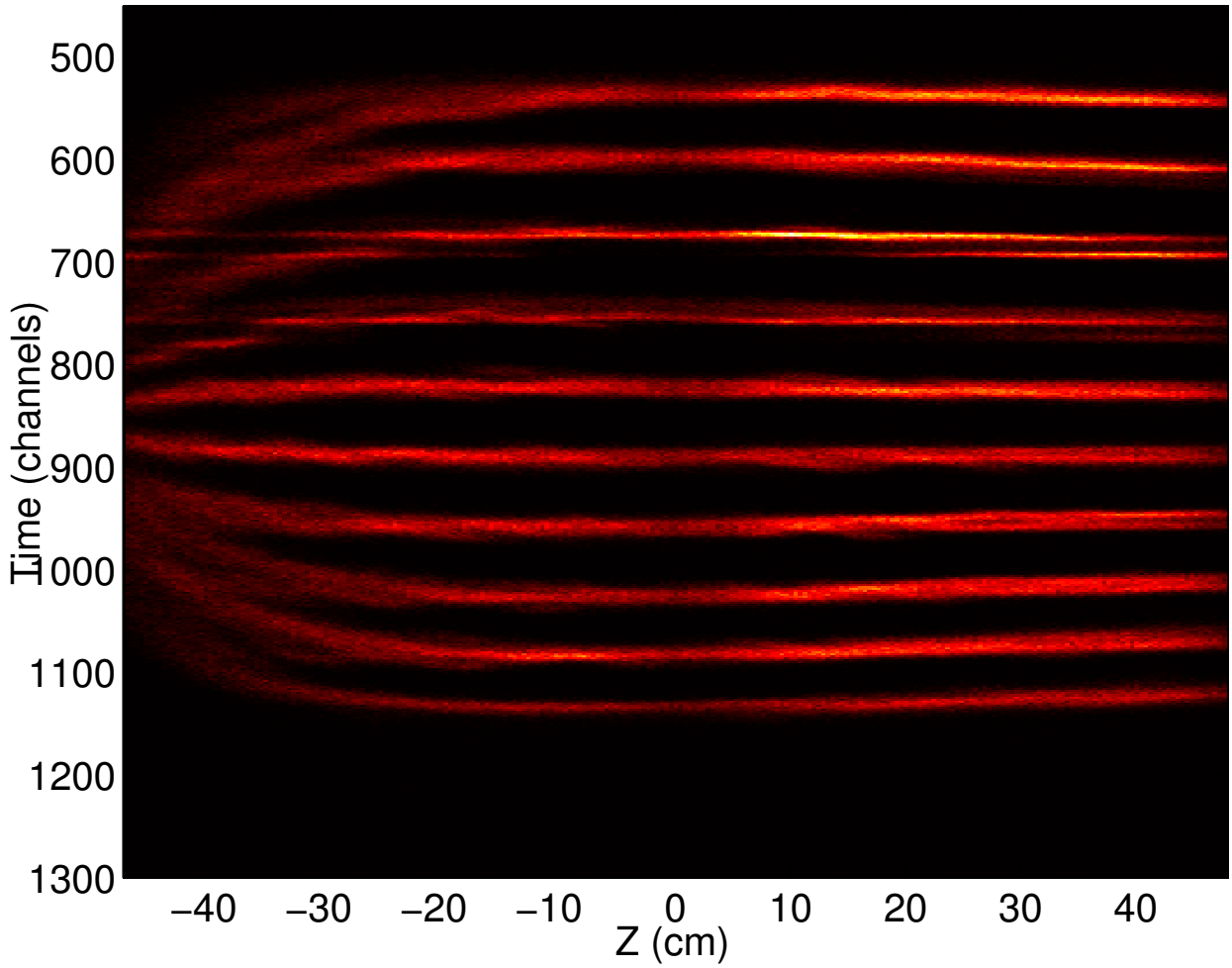

Figure 31: Correlation between the timing of signals and the corresponding location of neutron interactions along the length of the prototype detector. Each band represents events from one of the ten columns making up the detector module. These results, collected under uniform irradiation conditions, were used to calibrate the straw decoding scheme in the y-direction (see also Fig.33).

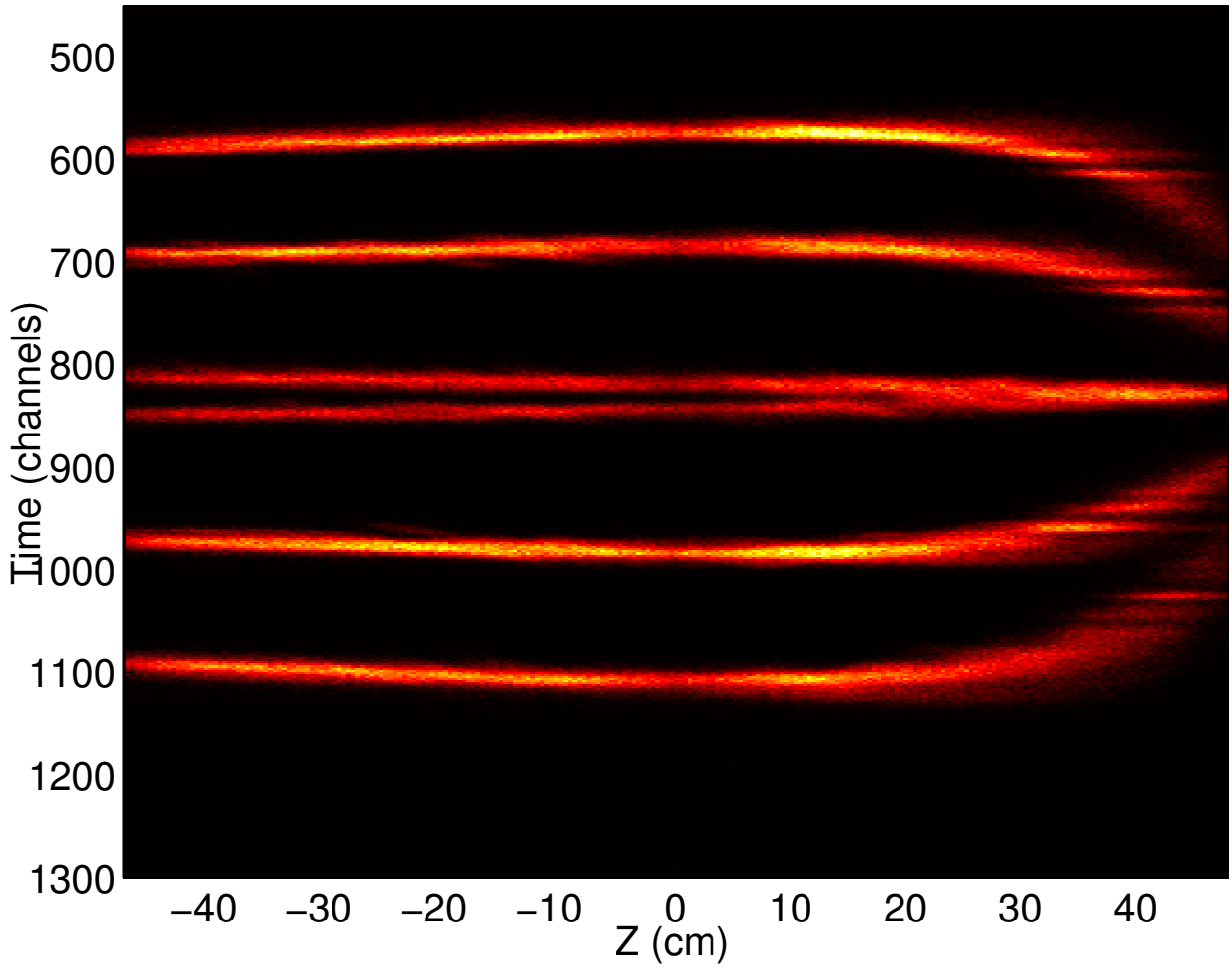

Figure 32: Correlation between the timing of signals and the corresponding location of neutron interactions along the length of the prototype detector. Each band represents events from one of the five rows making up the detector module. These results, collected under uniform irradiation conditions, were used to calibrate the straw decoding scheme in the x-direction (see also Fig.33).

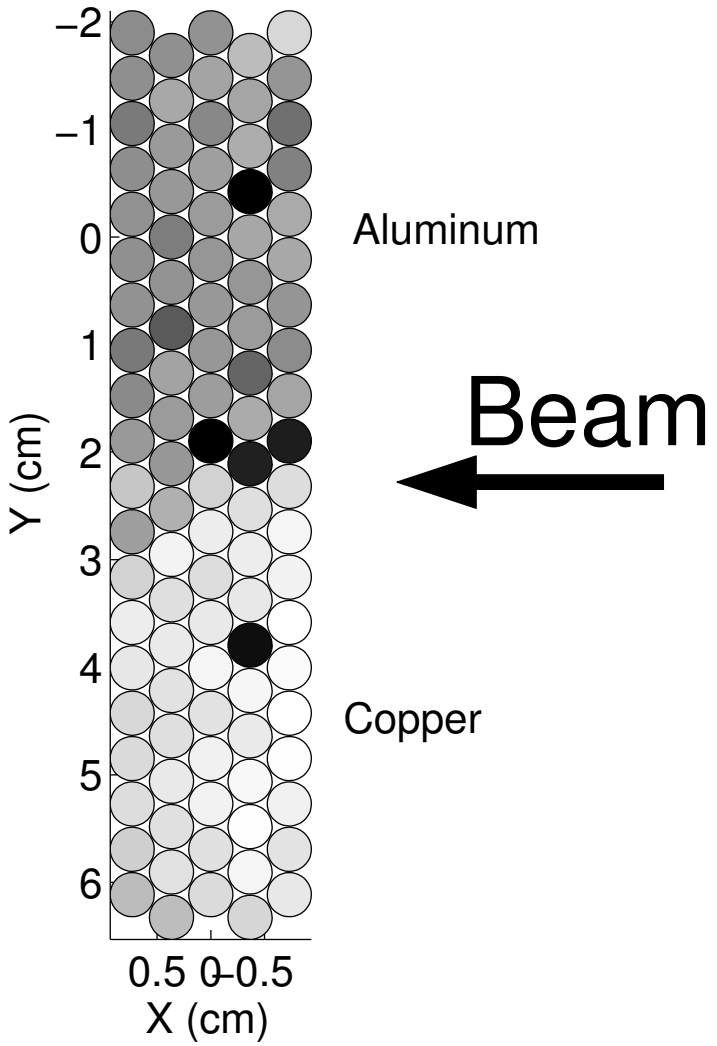

Figure 33: Cross-sectional view of both modules (copper and aluminum) in the prototype detector, showing the location of individual straws, and their sensitivity to uniform irradiation. The two modules were positioned adjacent to one another, as shown, with the neutron beam in the direction of the positive x-axis. A darker shade denotes a lesser sensitivity.

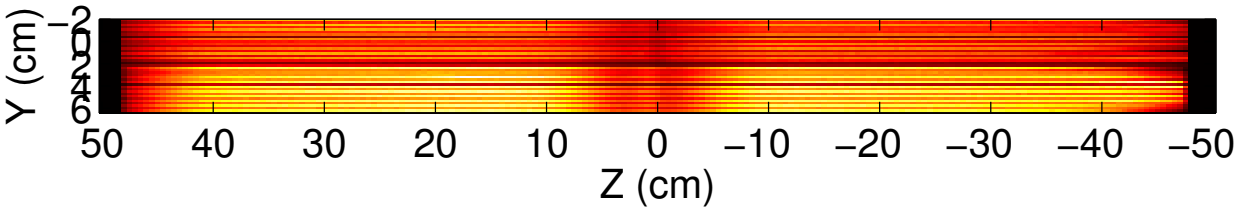

Figure 34: Two-dimensional image created with the detector face fully exposed (no collimator).

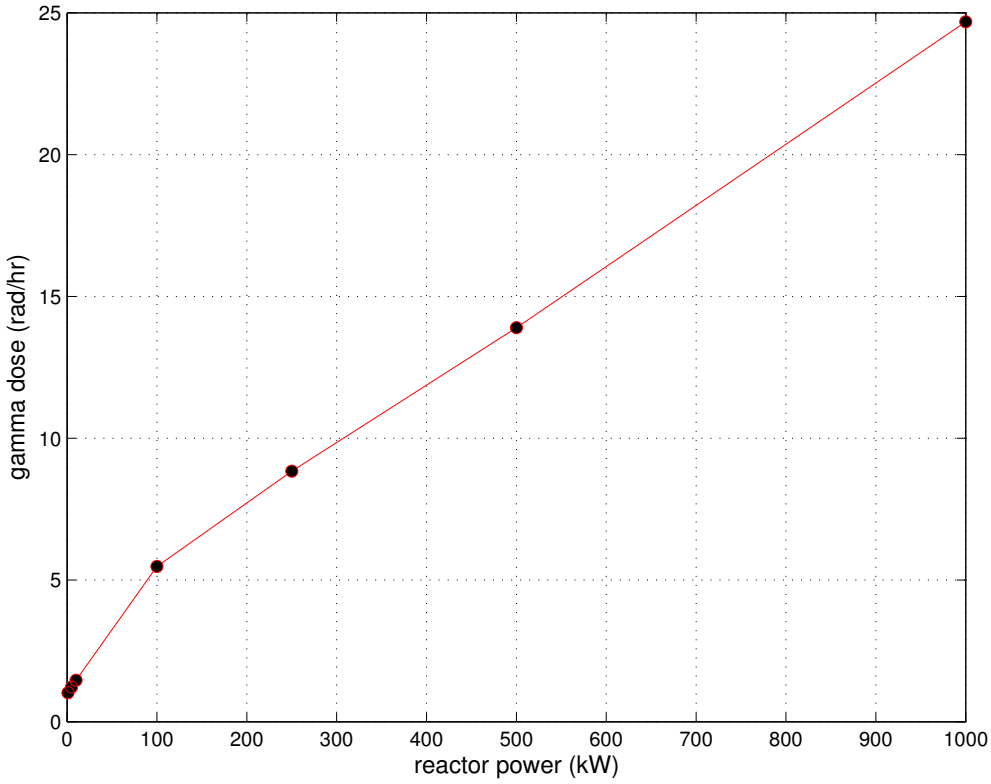

Figure 35: Gamma dose rate measured in the neutron beam at TAMU NSC.